Received December 2002
Revised January 2003
Accepted February 2003

An overview of advances in heat conduction models and approaches for prediction of thermal conductivity in thin dielectric films

Christianne V.D.R. Anderson
Department of Mechanical Engineering, University of Minnesota, Minneapolis, Minnesota, USA
Kumar K. Tamma
AHPCRC, Minneapolis, Minnesota, USA

Keywords *Thermal conductivity, Heat conduction, Dielectric properties*

Abstract *We first provide an overview of some predominant theoretical methods currently used for predicting thermal conductivity of thin dielectric films: the equation of radiative transfer, the temperature-dependent thermal conductivity theories based on the Callaway model, and the molecular dynamics simulation. This overview also highlights temporal and spatial scale issues by looking at a unified theory that bridges physical issues presented in the Fourier and Cattaneo models. This newly developed unified theory is the so-called C- and F-processes constitutive model. This model introduces the notion of a new dimensionless heat conduction model number, which is the ratio of the thermal conductivity of the fast heat carrier F-processes to the total thermal conductivity comprised of both the fast heat carriers F-processes and the slow heat carriers C-processes. Illustrative numerical examples for prediction of thermal conductivity in thin films are primarily presented.*

Introduction

Experimental measurements show that the thermal conductivity of very thin films is one to several orders of magnitude smaller than that of its bulk counterpart (Lambropoulos *et al.*, 1989). Many researchers have attempted to

The support in the form of computer grants from the Minnesota Supercomputer Institute (MSI) is gratefully acknowledged. The support in part, by Battelle/U.S.Army Research Office and the Army High Performance Computing Research Center (AHPCRC) under the auspices of the Department of the Army, Army Research Laboratory (ARL) under contract numbers DAAH04-96-6-0086 and DAAD19-01-2-0014 is also acknowledged. Also the authors would like to thank the help provided by extensive talks with Angela McConnell in helping clarify issues regarding the implementation of Holland's model. The Molecular Dynamics work has been implemented with the help of Deepak Srivastava at NASA Ames Research Center. Thanks are also due to Xiangmin Zhou for discussions in the C- and F-processes model for heat conduction. The content does not necessarily reflect the position or the policy of the government, and no official endorsement should be inferred.

International Journal of Numerical Methods for Heat & Fluid Flow
Vol. 14 No. 1, 2004
pp. 12-65

0961-5539
DOI 10.1108/09615530410511621

explain theoretically these experimental results. Fourier law, traditionally used to describe the behavior of macroscopic results, is unfortunately unable to duplicate accurately the experimental results at the microscale and nanoscale limits. This has opened the door to the field of microscale and nanoscale heat transfer. This paper provides an overview of the theoretical advancements with focus on heat conduction and the associated constitutive models, focusing on the prediction of thermophysical properties such as the thermal conductivity at small length scales.

Spatial and temporal regimes in heat conduction

Quantum mechanics has helped us to recognize that solids are composed of several discrete particles (electrons, neutrons and protons) at the microscopic level. Depending on the type of solid, different particles carry heat across the material in different ways and are therefore called heat carriers. Modeling the spatial and temporal regimes in materials can be broadly subdivided into four regimes (Zhigilei, 2002):

(1) macroscale;
(2) mesoscale;
(3) microscale; and
(4) nanoscale.

The characteristic lengths and times for these regimes are shown in Table I. In heat conduction, two major areas have been prominent:

(1) the *macroscale*, which involves the modeling of macroscale effects; and
(2) the *microscale*, which encompasses all the other regimes in materials modeling.

The macroscale formulation in heat conduction is based on the continuum assumption. It does not consider the size and time dependence of the heat transport. Heat is assumed to be carried by the atoms. The microscale formulation in heat conduction considers the physical mechanisms of heat transport through heat carriers where size and time dependence are crucial. This leads to the explanation of several parameters that characterize the microscopic regimes in both temporal and spatial regimes.

Regime	Characteristic length (m)	Characteristic time (s)
Macroscale	$\geq 10^{-3}$	$\geq 10^{-3}$
Mesoscale	$\sim 10^{-4}$-10^{-7}	$\sim 10^{-3}$-10^{-9}
Microscale	$\sim 10^{-6}$-10^{-8}	$\sim 10^{-8}$-10^{-11}
Nanoscale	$\sim 10^{-7}$-10^{-9}	$\sim 10^{-10}$-10^{-14}

Source: Zhigilei, (2002)

Table I.
Characteristic lengths and times in materials modeling

Microscopic in time – heat conduction. The important time parameters that govern the microscopic heat transport are (Goodson and Flik, 1992):

- the thermalization time – the time for the electrons and lattice to reach equilibrium;
- the diffusion time – the time taken by the heat information to travel through the specimen;
- the relaxation time – the time associated with the speed at which a thermal disturbance moves through the specimen;
- the heating time – the time that an external source heats the specimen; and;
- the physical process time – the total time duration of interest.

When the physical process time is comparable to any of the times described earlier, the time effect becomes important and the process is considered to be microscopic in time. When the heating time is of the order of the thermalization time, the energy deposition must be considered. The immediate question that naturally arises from this consideration is the following. Is the energy deposited in the lattice, the electron, or both? Finally, when the heating time is comparable to the diffusion time or the relaxation time, a finite speed of the thermal propagation must be considered.

Microscopic in size – heat conduction. The important size parameters that govern the heat transport in a specimen are (Goodson and Flik, 1992):

- the mean free path (λ); and
- the characteristic dimension of the material (L).

When the mean free path is much less than the characteristic dimension of the material ($\lambda \ll L$), the heat transport is said to be *macroscopic*. Fourier law is then applicable and the transport is governed by a purely diffusive nature. When the mean free path is of the order of or much greater than the characteristic dimension of the material ($\lambda \sim L$ or $\lambda \gg L$), the heat transport is said to be *microscopic*. Here, Fourier law breaks down and the transport shifts from a partially diffusive-ballistic to purely ballistic nature. These limits can be observed in Figure 1. The size effects of thermal conductivity were originally observed in 1938 in the experimental works of Haas and Biermasz, and the theoretical explanation shortly followed in the works of Casimir (Chen and Tien, 1993). Casimir identified that at the purely ballistic regime a temperature gradient could not be established, and according to the Fourier law, it was impossible to prescribe the thermal conductivity. At the purely ballistic limit, it was observed that the temperature at the boundaries, and not the temperature gradient within the film, governs the heat transport. Since thermodynamic equilibrium is restored due to the scattering of particles from the boundaries, the heat conduction by these particles is suggested to be similar to photons and can

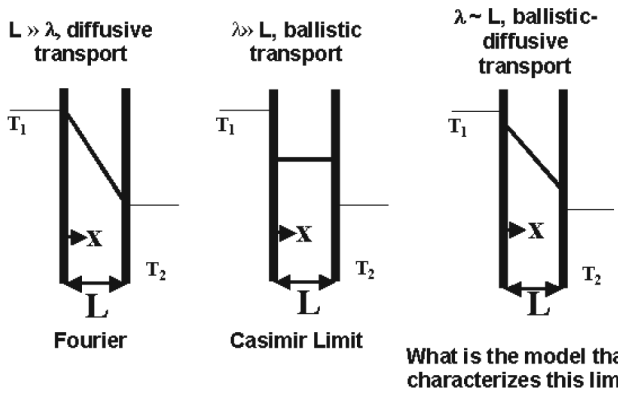

Figure 1.
Comparison of propagation methods

be analyzed as a radiative transfer model where the heat flux across the specimen can be described by:

$$q = \sigma\left(T_1^4 - T_2^4\right) \tag{1}$$

where σ is the Stefan-Boltzmann constant for the heat carrier, and T_1 and T_2 are the temperatures of the faces of a thin film. This is commonly referred to as the Casimir limit.

Prediction of thermal conductivity

Thermal conductivity is one of the hardest transport coefficients to calculate (Evans and Morriss, 1990). To date, several groups (Che *et al.*, 2000; Chen, 1997; Goodson *et al.*, 1995; Graebner *et al.*, 1994; Lambropoulos *et al.*, 1991; Lukes *et al.*, 2000; Majumdar, 1993; Maruyama, 2000; Osman and Srivastava, 2001; Schelling *et al.*, 2002; Volz and Chen, 1999) have chosen different approaches in order to predict the thermal conductivity of thin dielectric films, superlattices, nanowires and more recently nanotubes. These paths have their roots based on two major areas:

(1) the Boltzmann transport equation (BTE); and

(2) the molecular dynamics (MD) simulation.

The BTE has been extensively studied and has provided models shown to be appropriate for a class of thermal conductivity predictions at the microscopic level (Chen, 2000; Goodson *et al.*, 1995; Graebner *et al.*, 1994; Majumdar, 1993). However, more recently, the use of MD simulations for thermal conductivity prediction has been closely investigated (Lukes *et al.*, 2000; Maruyama, 2002; Osman and Srivastava, 2001; Schelling *et al.*, 2002; Volz and Chen, 1999). The focus of this section is to provide an overview of the two theories.

In the next section, we discuss three predominant approaches that have been derived from the BTE. The first two, the modified Callaway/Holland's models and the equation of phonon radiative transfer (EPRT), have previously been

used in the prediction of the thermal conductivity of thin dielectric films. The third is the newly developed C- and F-processes model which introduces the notion of a new dimensionless heat conduction model number. After discussing these approaches, we also present an overview of the MD simulation for thermal conductivity prediction of thin films and nanocarbon tubes.

BTE

The heart of heat transport theory is the BTE. The BTE determines the status of a particle via its location and velocity. The most general form of the BTE (Vincenti and Kruger, 1977) is given as

$$\frac{\partial f}{\partial t} + v \cdot \nabla f + a \cdot \frac{\partial f}{\partial v} = \left(\frac{\partial f}{\partial t}\right)_{\text{scatt}} \tag{2}$$

where $f(\vec{r}, T, \omega)$ is the non-equilibrium thermodynamic distribution function, $v(\omega)$ is the phonon velocity (that is, the speed of sound in dielectrics), $a(v)$ is the particle acceleration and t is time. The first term in equation (2) represents the net rate of particles over time, the second term is the convective inflow of particles in physical space, the third term is the net convective inflow due to acceleration in velocity space, and the term on the right hand side is the net rate of change of particles inside a control volume due to collisions. The phonon velocity in a dielectric material is fairly constant over a large frequency range, thus $\partial f/\partial v$ can be neglected. Both energy and temperature gradients tend to disturb the electron distribution, and this tendency is opposed by processes that restore equilibrium, such as the scattering of electrons or phonons by lattice vibrations and crystal defects. As a result, the scattering term is approximated under the relaxation-time approximation (Kittel, 1996) as,

$$\left(\frac{\partial f}{\partial t}\right)_{\text{scatt}} = \frac{\partial (f - f^0)}{\partial t} = \frac{f^0 - f}{\tau} \tag{3}$$

where $f^0(\vec{r}, T, \omega)$ is the thermodynamic distribution at equilibrium (Bose-Einstein distribution for boson particles (such as phonons), and Fermi-Dirac distribution for fermion particles (such as electrons), $\partial f^0/\partial t = 0$, and $\tau(\omega, v)$ is the rate of return to equilibrium and is called the relaxation time.

Kinetic theory is derived from the BTE under the premise that there is local thermal dynamic equilibrium (LTE) (Ashcroft and Mermin, 1976). In cases where LTE is not achieved, one solves the BTE. However, in the presence of a temperature gradient, the LTE is implied, and as an illustration of the one-dimensional diffusion term in equation (2), $\partial f/\partial x \sim \partial f^0/\partial x$, and the $\partial f/\partial x$ term can be approximated as (Callaway, 1959)

$$\frac{\partial f}{\partial x} = \frac{\mathrm{d}f^0}{\mathrm{d}T}\frac{\mathrm{d}T}{\mathrm{d}x} \tag{4}$$

The flux of particles is given by (Kittel, 1996)

$$q(x) = \int_0^{\omega_D} v_x f(x) \hbar \omega D(\omega)\, \mathrm{d}\omega \tag{5}$$

The transient one-dimensional BTE under the relaxation-time approximation and the temperature gradient approximation is given by

$$\frac{\partial f}{\partial t} + v_x \frac{\mathrm{d}f^0}{\mathrm{d}T}\frac{\mathrm{d}T}{\mathrm{d}x} = \frac{f^0 - f(x)}{\tau} \tag{6}$$

As the temperature of a material is increased or decreased, these particles interact and collide with each other in order to return the system back to thermodynamic equilibrium (the mean time associated with these scattering processes is the relaxation time (τ), and the mean distance associated with these scattering processes is the mean free path (λ)).

Solving the BTE is difficult. The relaxation-time approximation is a widely used simplification to its solution in thermal conductivity models. The following models based on the relaxation-time approximation have either been proposed or used to determine thermal conductivity in thin dielectric films:

- the newly proposed C- and F-processes model;
- the EPRT; and
- the modified Callaway/Holland's models.

Derivation of the C- and F-processes model and the generalized one-step temperature equation from the BTE. Another desire in the theoretical arena is to provide fundamental concepts that can explain and bridge the Fourier and Cattaneo limits. Beyond the ability to develop thermal conductivity models from the BTE, several phenomenological constitutive models have been physically explained by deriving from the BTE. Two of these models are the Fourier and Cattaneo models. In order to obtain these constitutive models from the BTE, the assumption that there exists a temperature gradient (implying thermodynamic equilibrium) within the medium is made in addition to the relaxation-time approximation (see equation (4)).

In an effort to provide a unified theory of heat conduction, the derivation of the C- and F-processes model is based on the hypothesis that upon the application of a temperature gradient, there simultaneously co-exist both slow and fast processes associated with the heat carriers. This results in a linear combination of the Fourier and Cattaneo "like' processes based on the original work by Tamma and Zhou (1998) but later extended by Zhou *et al.* (2001). This model separates the heat carriers governed by slow processes from those governed by fast processes at a reference threshold frequency. Hence, if we consider a threshold frequency ω_T, which is time dependent, in the early transient where low energy processes are separated from high energy processes, then the total heat flux given in equation (5) can be modified to account for the low-and high-energy processes as

$$q = \int_0^{\omega_T} v_x f(x) \hbar \omega D(\omega)\, d\omega + \int_{\omega_T}^{\omega_D} v_x f(x) \hbar \omega D(\omega)\, d\omega = q_C + q_F \quad (7)$$

where we postulate a threshold frequency such that the integral up to a threshold frequency ω_T involves the slow Cattaneo-like processes and yields a heat flux associated with the slow moving processes q_C (these processes are believed to dominate the process early on), and that the integral from the threshold to the Debye frequency, ω_D involves the fast Fourier-like processes and yields a heat flux associated with the fast moving processes q_F. The total heat flux (q) is the combination of the Cattaneo-like (q_C) and Fourier-like (q_F) heat fluxes.

In this regard, the transient BTE can be multiplied by $v_x \hbar \omega D(\omega)$ and integrated over the two separate frequency ranges yielding the following two equations which are associated with the C-processes (Cattaneo-like) and the F-processes (Fourier-like):

$$\int_0^{\omega_T} v_x \hbar \omega D(\omega) \frac{\partial f}{\partial t}\, d\omega + \int_0^{\omega_T} v_x^2 \hbar \omega D(\omega) \frac{\partial f}{\partial x}\, d\omega = \int_0^{\omega_T} v_x \hbar \omega D(\omega) \left(\frac{f^0 - f}{\tau} \right) d\omega \quad (8)$$

and

$$\int_{\omega_T}^{\omega_D} v_x \hbar \omega D(\omega) \frac{\partial f}{\partial t}\, d\omega + \int_{\omega_T}^{\omega_D} v_x^2 \hbar \omega D(\omega) \frac{\partial f}{\partial x}\, d\omega = \int_{\omega_T}^{\omega_D} v_x \hbar \omega D(\omega) \left(\frac{f^0 - f}{\tau} \right) d\omega \quad (9)$$

In support of this hypothesis, next consider the Maxwell-Boltzmann, Bose-Einstein, and Fermi-Dirac distribution functions shown in Figure 2 where the Fermi energy is set to zero. At high frequencies (or energies), the

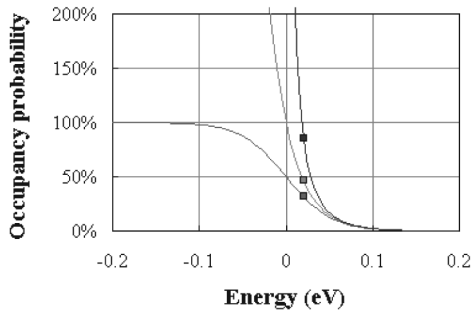

Source: Adapted from Zeghbroeck (1996)

Figure 2.
Occupancy probability for the Fermi-Dirac, the Bose-Einstein and the Maxwell-Boltzmann distributions

effect of the Fermi-Dirac and the Bose-Einstein statistical functions are eliminated and all distributions converge to a Maxwell-Boltzmann distribution. *At high frequencies the wavelength of the particle is short and the statistical distinction is unimportant*. Because of this statistical unimportance, it is reasonable to assume that the term

$$\int_{\omega_T}^{\omega_D} v_x \hbar \omega D(\omega) \frac{\partial f}{\partial t} \, d\omega = 0,$$

due to the observation that the distribution function is fairly constant over time for high frequencies. In other words, as the different distribution functions reach their equilibrium positions, most of the change in the distribution functions occurs at the lower frequencies, and the distributions at the high frequency tail are fairly constant over time. Hence, the df/dt term in equation (9) is neglected.

Also note that as time evolves, the threshold frequency must change as the distributions reach these equilibrium stages. This is a similar analogy to the change of the Fermi energy with temperature (Lee *et al.*, 1973).

Now consider the notion of a non-dimensional heat conduction model number, F_T, which is physically depicted as (Tamma and Zhou, 1998)

$$F_T = \frac{K_F}{K_F + K_C} \tag{10}$$

where K_F is the conductivity due to the fast F-processes and K_C is the conductivity due to the slow C-processes.

Further, the following is defined

$$K = \int_0^{\omega_T} v_x^2 \tau \frac{df^0}{dT} \hbar \omega D(\omega) \, d\omega + \int_{\omega_T}^{\omega_D} v_x^2 \tau \frac{df^0}{dT} \hbar \omega D(\omega) \, d\omega = K_C + K_F \tag{11}$$

Next, introducing the non-dimensional heat conduction model number as the following ratio, we have

$$F_T = \frac{\int_{\omega_T}^{\omega_D} v_x^2 \tau \frac{df^0}{dT} \hbar \omega D(\omega) \, d\omega}{\int_0^{\omega_D} v_x^2 \tau \frac{df^0}{dT} \hbar \omega D(\omega) \, d\omega} \tag{12}$$

Upon application of the heat flux of particles given in equation (7) and the thermal conductivity given in equation (11), equations (8) and (9) can be reduced to the Fourier and Cattaneo processes as

$$q_F = -K_F \frac{dT}{dx} \tag{13}$$

$$q_C + \tau \frac{dq_C}{dt} = -K_C \frac{dT}{dx} \tag{14}$$

where the total heat flux, q, is given as $q = q_C + q_F$.

When the definition from equation (12) is introduced into these two previous equations, then equations (7)-(9) finally yield the C- and F-processes heat conduction constitutive model in terms of the heat conduction model number as,

$$q = q_F + q_C \tag{15}$$

$$q_F = -F_T K \frac{dT}{dx} \tag{16}$$

$$q_C + \tau \frac{dq_C}{dt} = -(1 - F_T) K \frac{dT}{dx} \tag{17}$$

Alternatively, one could consider an underlying viewpoint as related to non-equilibrium situations that could be implied in the C- and F-processes model as follows:

$$T_F = F_T T \tag{18}$$

$$T_C = (1 - F_T) T \tag{19}$$

where the total temperature, T, is given by $T = T_F + T_C = F_T T + (1 - F_T) T$.

Substituting these equations into the C- and F-processes model leads to the notion of a non-equilibrium model:

$$q = q_F + q_C \tag{20}$$

$$q_F = -K \frac{dT_F}{dx} \tag{21}$$

$$q_C + \tau \frac{dq_C}{dt} = -K \frac{dT_C}{dx} \tag{22}$$

In general, the C- and F-processes heat conduction constitutive model is given by

$$\mathbf{q}_F = -K_F \nabla T = -F_T K \nabla T = -K \nabla T_F \tag{23}$$

$$\mathbf{q}_{\mathrm{C}} + \tau \frac{\partial \mathbf{q}_{\mathrm{C}}}{\partial t} = -K_{\mathrm{C}} \nabla T = -(1 - F_{\mathrm{T}}) K \nabla T = -K \nabla T_{\mathrm{C}} \tag{24}$$

$$\mathbf{q} = \mathbf{q}_{\mathrm{F}} + \mathbf{q}_{\mathrm{C}} \tag{25}$$

which explains the present derivation based on fundamental physical principles emanating from the BTE.

In the above equations, $\mathbf{q}$ is the total heat flux due to the mechanism of heat conduction (which is comprised of that associated with each of the Fourier-type fast and Cattaneo-type slow processes), and K is the total conductivity which is the sum of the Fourier (effective) conductivity, K_{F}, and the Cattaneo (elastic) conductivity, K_{C}. Thus, $K = K_{\mathrm{F}} + K_{\mathrm{C}}$.

Also, $F_{\mathrm{T}} \in [0, 1]$ are the strict bounds which were introduced (Tamma and Zhou, 1998) in the definition of each of the heat flux constitutive processes characterizing the process of heat transport with evolution of time and termed as the *macroscale heat conduction model number* whose physics should strictly be adhered to and was defined earlier.

Note that the subscripts F and C pertain to the F-and C-processes and the model acknowledges the co-existence of both finite and infinite speeds of propagation of the thermal disturbances simultaneously.

Also note that when $F_{\mathrm{T}} \in (0, 1)$, the combined representation of the C- and F-processes model leads to the Jeffreys-type model; when ($F_{\mathrm{T}} = 0$), the C- and F-processes model naturally reduces to the Cattaneo model; and when ($F_{\mathrm{T}} = 1$), the C- and F-processes model naturally reduces to the Fourier model (this is unlike the Jeffreys model which only reduces to a Fourier-like model).

As such, the proposition is that very early in the transient, the Cattaneo type slow processes dominate, and subsequently with the passage of time, the Fourier type fast processes dominate the heat conduction process. The heat transport characterized by F_{T} strictly varies with time starting from zero and leading to a value of unity.

Note that the combined form of equations (16) and (17) leads to the Jeffreys model and the associated temperature operator. In 1989, Joseph and Preziosi (1989) correlated a theory from viscoelasticity to heat transfer. By substituting the combined form of equations (16) and (17) into the energy equation, the Generalized One-Step temperature formulation is obtained as

$$\frac{1}{c_T^2} \frac{\partial^2 T}{\partial t^2} + \frac{1}{\alpha} \frac{\partial T}{\partial t} = \frac{\partial^2 T}{\partial x^2} + \frac{1}{K} \left(S + \tau \frac{\partial S}{\partial t} \right) + \tau F_{\mathrm{T}} \frac{\partial}{\partial t} \left(\frac{\partial^2 T}{\partial x^2} \right) \tag{26}$$

where the temperature propagation speed is given by $c_{\mathrm{T}} = \sqrt{K/\rho C \tau}$ and α is the thermal diffusivity.

It is interesting to mention that Majumdar (1993) has shown that the Cattaneo model, which has been used to describe a heat propagation due to a wave, is derived from the BTE by making the temperature gradient

assumption that leads to Fourier law. The Cattaneo model is valid microscopically for small time scales but it is not appropriate for use with very thin films.

At the same time the C- and F-processes model was developed, Chen (2001) independently developed the ballistic-diffusive (BD) model. It is noteworthy to mention that analogous assumptions made to derive the C- and F-processes model are made to derive the BD model. The assumptions in the original work described by Tamma and Zhou (1998) treat the total distribution function by splitting it into two contributions. Aspects of the derivation of the C- and F-processes model is based on the temperature gradient assumption (the derivation of the BD model is also based on the temperature gradient assumption). While the C- and F-processes model provides accurate results for small timescales and macroscopic material sizes, in light of recent results obtained by the BD model (Chen, 2001; Yang and Chen, 2001), the C- and F-processes model may also hold for microscopic material sizes, something that is currently being investigated and we hope to disseminate relevant issues in the near future.

EPRT. In thin dielectric films, the major heat carriers are phonons. The thermodynamic equilibrium distribution for these carriers follows the Bose-Einstein distribution, which is similar to the distribution of photons. Under this premise the EPRT is originally described by Majumdar (1991) based on the correlation between the radiation theory (i.e. the equation of radiative transfer (ERT) and the transport theory in dielectric thin films. The major assumption made in solving the transport properties in very thin films is that the problem can be solved as a one-dimensional gray medium between black walls at specified temperatures under radiative equilibrium. This condition arises when a dielectric film is sandwiched between two metallic films. The following is a detailed derivation of this theory.

The intensity of photons, that is, the radiation emitted in any direction by a wave packet, is given by (Vincenti and Kruger, 1977)

$$I(\theta, \phi, \omega, x, t) = \sum_{p} v(\theta, \phi) f(x, t) \hbar \omega D(\omega), \tag{27}$$

where the summation is over the photon polarizations, $v(\theta,\phi)$ is the velocity vector in the direction of θ and ϕ within a unit solid angle, $\hbar\omega$ is the energy at which the photons propagate and $D(\omega)$ is the density of states per unit volume. The frequency dependency of the phonon intensity is eliminated by assuming that the film medium acts as a gray body.

For cases where $\lambda \gg$ L, the EPRT appears to model microscale aspects in both time- and scale-limits. In these cases, the thermal conductivity for thin films is obtained at steady-state due to scattering of phonons from the boundaries, which returns the system to thermodynamic equilibrium. This suggests that the heat conduction by phonons is similar to that of photons and

thus can be analyzed as a radiative transfer problem (Ashcroft and Mermin, 1976, pp. 466-7).

Applying the analogy between photons and phonons and multiplying equation (6) by $v_x \hbar\omega D(\omega)$ and using the intensity definition (equation (27), the EPRT is obtained as

$$\frac{\partial I(x,\mu)}{\partial t} + v_x \frac{\partial I(x,\mu)}{\partial x} = \frac{I^0(T(x)) - I(x,\mu)}{\tau} \tag{28}$$

where the velocity is in the direction of the phonon propagation $v_x = v\mu$, and $\mu = \cos\theta$, θ is the angle between the phonon propagation and the x-direction, and I^0 is the equilibrium intensity.

At steady-state, equation (28) reduces to

$$v\mu\tau \frac{\partial I(x,\mu)}{\partial x} + I(x,\mu) = I^0(T(x)) \tag{29}$$

At this point, this equation has two unknowns, $I(x, \mu)$ and $I^0(T(x))$. For steady state, it is possible to reach a state of *phonon radiative equilibrium* where $\nabla \cdot \vec{q} = 0$. Integrating equation (29) over all directions $(-1 < \mu < 1)$ and all frequencies, we have

$$\int_{\mu=-1}^{\mu=1} \int_{\omega=0}^{\omega=\omega_D} \left(v\mu\tau \frac{\partial I(x,\mu)}{\partial x} + I(x,\mu) \right) \mathrm{d}\omega \, \mathrm{d}\mu = \int_{\mu=-1}^{\mu=1} \int_{\omega=0}^{\omega=\omega_D} I^0(T(x)) \, \mathrm{d}\omega \, \mathrm{d}\mu \tag{30}$$

The total radiation flux is expressed in terms of the intensity as (Sparrow, 1991, p. 212)

$$q(x) = 2\pi \int_{-1}^{1} \int_{0}^{\omega_D} \mu I(x,\mu) \, \mathrm{d}\omega \, \mathrm{d}\mu \tag{31}$$

Hence, the first term in equation (30) is

$$\frac{v\tau}{2\pi} \frac{\mathrm{d}q}{\mathrm{d}x}$$

and under radiative equilibrium it is zero. Since I^0 is analogous to the blackbody intensity and is independent of direction, equation (30) yields

$$\int_{\mu=-1}^{\mu=1} \int_{\omega=0}^{\omega=\omega_D} \left(I(x,\mu) \right) \mathrm{d}\omega \, \mathrm{d}\mu = 2 \int_{\omega=0}^{\omega=\omega_D} I^0(T(x)) \, \mathrm{d}\omega \, \mathrm{d}\mu \tag{32}$$

By simplification, equation (32) provides I^0 as

$$I^0(T(x)) = \frac{1}{2}\int_{\mu=-1}^{\mu=1}\int_{\omega=0}^{\omega=\omega_D} (I(x,\mu))\,\mathrm{d}\omega\,\mathrm{d}\mu \tag{33}$$

For temperatures lower than the Debye temperature the total blackbody intensity is given by the Stefan-Boltzmann law and I^0 is found to be

$$I^0(T(x)) = \frac{\sigma}{\pi}T^4(x) \tag{34}$$

where σ is the Stefan-Boltzmann constant.

The Stefan-Boltzmann constant was calculated for phonons as (Swartz and Pohl, 1989)

$$\sigma = \frac{\pi^2}{40}\frac{k_B^4}{\hbar^3 v^2} \tag{35}$$

where k_B is the Boltzmann constant, $\hbar$ is Planck's constant divided by 2π, and v is the speed of sound in solids. The Stefan-Boltzmann constant can also be related to the specific heat as (Majumdar, 1993)

$$\sigma = \frac{Cv}{16T^3} \tag{36}$$

When substituting the form of equation (34) into equation (29) the form of the traditional and well known ERT is recovered where the medium is assumed to absorb energy under radiative equilibrium with isotropic scattering (Özisik, 1973; Siegel and Howell, 1992).

The outside walls of the film are assumed to be black at specified temperatures. This assumption is made since the dielectric material of real solid-state devices, which may be comprised of several layers of films, is between different metallic films. In metallic films the electron-phonon mean free path is much smaller than the phonon mean free path in the dielectric films. This leads to the assumption of thermalizing black boundaries at fixed temperatures. The boundary conditions used for single thin film analysis are

$$I^+(0,\mu) = \frac{\sigma T_0^4}{\pi} \tag{37}$$

$$I^-(L,\mu) = \frac{\sigma T_L^4}{\pi} \tag{38}$$

where σ is the Stefan-Boltzmann constant of the dielectric film, T_0 is the temperature at location $x = 0$, and T_L is the temperature at the location $x = L$.

Majumdar (1993) analyzed the EPRT for both acoustically thin ($\lambda \gg L$) and acoustically thick ($\lambda \ll L$) limits and shows that the EPRT does indeed provide results that span both limiting cases where the Casimir and the Fourier laws are applicable.

Determination of the scattering mechanisms used in the EPRT. Heat conduction in solids is well understood to follow the *kinetic formula*

$$K = \frac{1}{3} C v_s \lambda \tag{39}$$

where K the thermal conductivity of an ensemble of heat carriers is given by the total specific heat C, the average speed of the heat carriers v_s, and the mean free path λ. The focus of this discussion is the thermal conduction of insulators thus the heat carries of interest are phonons. Therefore, C is given by the Debye formula, v_s is the average velocity of sound which can be obtained from phonon spectrums, and the problematic λ can be obtained based on the discussion below (note that the relaxation time is related to the mean free path as $\lambda = v_s \tau$).

The overall trend in the determination of thermal conductivity as a function of temperature is limited by the dependence of the scattering rates on temperature. At high temperatures, the mean free path $\lambda \propto 1/T$. If v_s is assumed independent of temperature, then at high temperatures (well above the Debye temperature), the specific heat is constant and we obtain the thermal conductivity of a phonon, $K_{ph} \propto 1/T$. However, the coefficient of proportionality is difficult to determine (Ziman, 1960). At low temperatures, the phonon-phonon scattering becomes unimportant and the mean free path is limited by scattering with lattice defects where $\lambda = \lambda_{impurities}$ which is independent of temperature. Since v_s is also independent of temperature, C is proportional to T^3, and hence K is proportional to T^3 at low temperatures as shown in Figure 3.

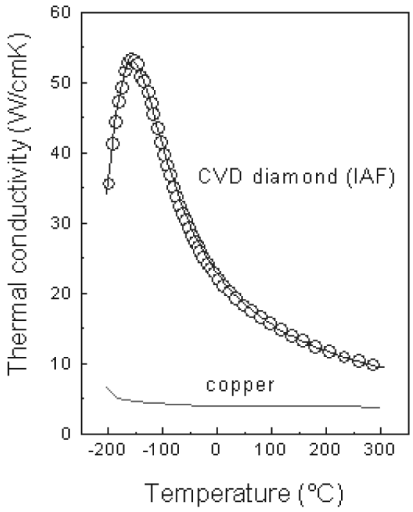

Source: http://www.iaf.fhg.de/budiprth/frames-e.htm

Figure 3.
Schematic of thermal conductivity of CVD diamond heat spreader prepared at the Fraunhofer Institute (IAF). Comparison of thermal conductivity of copper and diamond at high and low temperature approximations

If the thermal conductivity of a material is known, it can be used to extract the mean free path of thin films via the kinetic formula. This method is fairly simple and can provide a quick estimation of the mean free path (Chen and Tien, 1993-Chen, 1998). Therefore, the estimation of the λ can be performed from known bulk thermal conductivity values. However, this estimation of the mean free path assumes that all phonons have the same energy and velocity.

Table II provides the prediction of λ for a few dielectric materials under the Debye approximation at room temperature. For amorphous materials, such as SiO_2, the Debye approximation is used, however, care must be taken since its validity is still under extensive study (Zeng and Chen, 2001).

Finite element formulation of the EPRT. The steady-state form of the EPRT under radiative equilibrium is given by

$$v\mu_i\tau\frac{\partial I(x_j,\mu_i)}{\partial x_j}+I(x_j,\mu_i)=\frac{1}{2}\int_{-1}^{1}I(x_j,\mu_i^*)\,\mathrm{d}\mu^* \tag{40}$$

where $I(x_j, \mu_i)$ is the intensity of the phonon as a function of position x, and direction μ, $\mu = \cos\theta$, θ is the angle of different directions of I (θ ranges from 0 to 180°), and μ^* is just a dummy variable of integration.

The integral on the right hand side of equation (40) is approximated by Gaussian quadrature as (Kumar *et al.*, 1990)

$$I^0(T(x))=\int_{-1}^{1}I(x_j,\mu_i^*)\,\mathrm{d}\mu^*=\sum_{k=1}^{\mathrm{NGP}}I_j(\mu_k)w_k \tag{41}$$

where μ_k are the discrete directions and w_k the weighting factors. In a study, conducted by Kumar *et al.* (1990), there are eight recommended directions, therefore 16 Gauss points are used (eight Gauss points for the positive μ directions and eight Gauss points for the negative μ directions). These data are presented in Table III.

The ERT is well documented in radiation textbooks (Özisik, 1973; Siegel and Howell, 1992; Sparrow, 1991). Özisik (1973) describes that the ERT has been derived previously from the BTE and control volume techniques. Based on similar development as the ERT, equation (29) can be written under the two-flux model of radiative transfer as separate "+" and "−" contributions (Siegel and Howell, 1992)

Material	Specific heat $\times 10^6$ (J/m^3 K)	Velocity (m/s)	λ (Å)
Si	1.66	6,400	409
Ge	1.67	3,900	275
GaAs	1.71	3,700	208
SiO_2	1.687	4,400	5.58
Diamond	1.81	13,500	3,929

Source: Chen (2000) and Zeng and Chen (2001).

Table II.
Phonon properties at room temperature based on the Debye model

$$v\tau\mu\frac{\partial I^{+}(x,\mu)}{\partial x}+I^{+}(x,\mu)=I^{0}(T(x)) \tag{42}$$

and

$$v\tau\mu\frac{\partial I^{-}(x,\mu)}{\partial x}+I^{-}(x,\mu)=I^{0}(T(x)) \tag{43}$$

where equation (42) is valid for $\mu > 0$ and equation (43) for $\mu < 0$. Note that the term $v\tau$ is the definition for mean free path (λ).

The finite-element method (FEM) has been previously employed to solve pure radiation problems, and Razzaque *et al.* (1984) have modeled the ERT for a particular two-dimensional case. However, the FEM has not been implemented in the literature for the present form of the EPRT and recent efforts have been described by Anderson and Tamma (2002). Assuming a linear approximation for the intensity, $I = N_j I_j$, the Galerkin FEM is applied to equation (30) as

$$\int_0^h W_j(x_j)v\mu_i\tau\frac{\partial I(x_j,\mu_i)}{\partial x_j}\,\mathrm{d}x+\int_0^h W_j(x_j)I(x_j,\mu_i)\,\mathrm{d}x$$

$$=\int_0^h W_j(x_j)\left(\frac{1}{2}\int_{-1}^{1}I(x_j,\mu_i^{*})\,\mathrm{d}\mu^{*}\right)\mathrm{d}x \tag{44}$$

where $W_j(x_j)$ is the weighting function and is assumed as $W_j(x_j) = N_j$, where N_j are the shape functions. For a two-noded linear element of size h,

$$N_j=\begin{bmatrix}N_1 & N_2\end{bmatrix} \tag{45}$$

where $N_1 = 1 - (x/h)$ and $N_2 = x/h$. Note that the right hand side of equation (44) is approximated by Gaussian quadrature (equation (41)) which gives values at each node and is a constant for each direction. Because the FEM is formulated on an elemental basis the nodal values are averaged to obtain a constant value for the element. Therefore,

Location (μ_i)	Weight (w_i)
±0.095012509837637	0.189450610455068
±0.281603550779258	0.182603415044923
±0.458016777657227	0.169156519395002
±0.617876244402643	0.149595988816576
±0.755404408355003	0.124628971255533
±0.865631202387831	0.095158511682492
±0.944575023073232	0.062253523938647
±0.989400934991649	0.027152459411754

Table III.
Data used for 16 Gauss points in Gaussian quadrature

$$\frac{1}{2}\int_{-1}^{1} I(x_j, \mu_i^*)\, \mathrm{d}\mu^*$$

is reduced to I_1^0 and I_2^0 for a two-noded linear finite-element and the constant for the element is taken to be the average value $(I_1^0 + I_2^0)/2$.

Introducing the elemental constant into the right hand side of equation (44), the space-discretized representation yields

$$\int_0^h N_k v\mu_i \tau \frac{\partial N_j}{\partial x_j}\, \mathrm{d}x I_j + \int_0^h N_k N_j\, \mathrm{d}x I_j = \int_0^h N_k \left(\frac{I_1^0 + I_2^0}{2}\right) \mathrm{d}x \tag{46}$$

For a typical two-noded linear element, for $\mu_i > 0$, we have

$$\left[\frac{v\mu_i\tau}{2}\begin{bmatrix} -1 & 1 \\ -1 & 1 \end{bmatrix} + \frac{h}{6}\begin{bmatrix} 2 & 1 \\ 1 & 2 \end{bmatrix}\right]\begin{pmatrix} I_1^+(x_1, \mu_i) \\ I_2^+(x_2, \mu_i) \end{pmatrix} = \left(\frac{I_1^0 + I_2^0}{2}\right)\frac{h}{2}\begin{bmatrix} 1 \\ 1 \end{bmatrix} \tag{47}$$

Similarly for $\mu_i < 0$, we have

$$\left[\frac{v\mu_i\tau}{2}\begin{bmatrix} -1 & 1 \\ -1 & 1 \end{bmatrix} + \frac{h}{6}\begin{bmatrix} 2 & 1 \\ 1 & 2 \end{bmatrix}\right]\begin{pmatrix} I_1^-(x_1, \mu_i) \\ I_2^-(x_2, \mu_i) \end{pmatrix} = \left(\frac{I_1^0 + I_2^0}{2}\right)\frac{h}{2}\begin{bmatrix} 1 \\ 1 \end{bmatrix} \tag{48}$$

where h is the element size.

These equations are next solved for each direction (eight for $\mu_i > 0$ and eight for $\mu_i < 0$). After determining the energy intensity at all locations, the heat flux (equation (31)) and temperature (equation (34)) distribution profiles for a single thin film are obtained by employing

$$q(x_j) = 2\pi \sum_{i=1}^{8} \mu_i \left(I_{i,j}^+ w_i - I_{i,j}^- w_i\right) \tag{49}$$

and

$$T(x_j) = \left(\frac{\pi}{2\sigma}\sum_{i=1}^{8}\left(I_{i,j}^+ w_i + I_{i,j}^- w_i\right)\right)^{\frac{1}{4}} \tag{50}$$

For the cases analyzed, radiative equilibrium is assumed and to assess the accuracy of the solution, the heat flux across the film must be constant (Jen and Chieng, 1998; Majumdar, 1993) due to the radiative equilibrium assumption.

Finally, an effective thermal conductivity is obtained by invoking the form of Fourier law (Jen and Chieng, 1998)

$$K_{\text{eff}} = \frac{q(x_j)L}{T_0 - T_L} \tag{51}$$

where L is the thickness of the film, and T_0 and T_L are the imposed temperatures at the top and bottom surfaces of the film, respectively.

Owing to the nature of the first term on the left hand side in equations (47) and (48), numerical oscillatory behavior is observed and in order to stabilize these oscillations, the number of elements used was increased. As the thickness of the film is increased, the mesh needs to be refined. Unfortunately, known procedures to stabilize such numerical oscillations as in convective flow problems (i.e. upwinding) are not as straightforward for the first-order integrodifferential EPRT. Further study in this area is currently underway. Nonetheless, in this study a refined mesh was used as appropriate to yield satisfactory results. The computational procedure for typical finite-difference and FEMs is shown in Figure 4.

Callaway/Holland's model. When the assumption that all phonons have the same energy and velocity is not desired, it is possible to account for the phonon dispersion where C, v, and λ are frequency dependent. Equation (39) can be

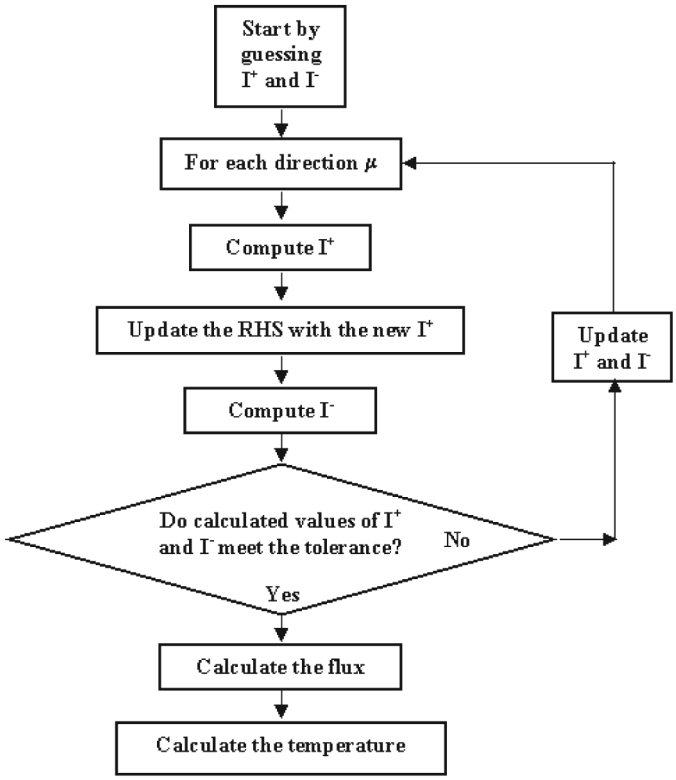

Figure 4.
Computational procedure for the numerical methods used for solving the EPRT for thin single films

modified by including the summation over all phonon branches (one longitudinal and two transverse) and by integrating over the phonon spectrum width of each branch as presented in the early works of Peierls in 1929,

$$K = \frac{1}{3}\sum_{p}\int C(\omega)v(\omega)\lambda(\omega)\,\mathrm{d}\omega \tag{52}$$

The temperature-dependent thermal conductivities of silicon and germanium films can be modeled based on the approximated solutions to the BTE where the frequency-dependent relaxation times represent the phonon scattering events. The most widely used model for determining the thermal conductivity is a method first proposed by Callaway (1959) which assumes that the N-processes dominate the scattering and the total thermal conductivity can be expressed as a sum of K_1 and K_2

$$K_1 = HT^3\int_0^{\theta_{\mathrm{D}/T}} J_4(x)\tau_{\mathrm{c}}(x)\,\mathrm{d}x \tag{53}$$

$$K_2 = HT^3\frac{\left(\int_0^{\theta_{\mathrm{D}/T}} J_4(x)\tau_{\mathrm{c}}(x)(\tau_{\mathrm{N}}(x))^{-1}\,\mathrm{d}x\right)^2}{\int_0^{\theta_{\mathrm{D}/T}} J_4(x)\tau_{\mathrm{c}}(x)(\tau_{\mathrm{N}}(x)\tau_{\mathrm{R}}(x))^{-1}\,\mathrm{d}x} \tag{54}$$

with

$$H = \frac{k_{\mathrm{B}}^4}{2\pi^2\hbar^3 v_{\mathrm{s}}};\quad \frac{1}{\tau_{\mathrm{c}}} = \frac{1}{\tau_{\mathrm{N}}} + \frac{1}{\tau_{\mathrm{R}}};\quad x = \frac{\hbar\omega}{k_{\mathrm{B}}T};\quad J_4(x) = \frac{x^4\,\mathrm{e}^x}{(\mathrm{e}^x-1)^2}$$

where τ_{c}^{-1} is the combined relaxation rate which is the sum of normal (N) and all resistive (R) scattering rates, θ_{D} the Debye temperature, x dimensionless phonon angular frequency, ω the phonon angular frequency, T the temperature, k_{B} the Boltzmann constant (1.3807×10^{-23} J/K), and $\hbar$ is the Planck's constant divided by 2π (1.05459×10^{-34} J s). Note that K_1 is the Debye model and K_2 is the addition of the thermal resistivity when N-processes are assumed to dominate the scattering (Berman, 1992).

The first modified form of Callaway's model, known as Holland's model (Holland, 1963), assumes that $K_2 = 0$ and includes the three phonon polarizations in K_1

$$K_1 = K_{\mathrm{TO}} + K_{\mathrm{TU}} + K_{\mathrm{L}} \tag{55}$$

where

$$K_{\mathrm{TO}} = \frac{2}{3}\int_0^{\theta_{\mathrm{TO}}/T} C_{\mathrm{T}}T^3\tau_{\mathrm{TO}}(x)J_4(x)\,\mathrm{d}x \tag{56}$$

$$K_{\mathrm{TU}} = \frac{2}{3}\int_{\theta_{\mathrm{TO}}/T}^{\theta_{\mathrm{TU}}/T} C_{\mathrm{T}} T^3 \tau_{\mathrm{TU}}(x) J_4(x)\,\mathrm{d}x \tag{57}$$

$$K_{\mathrm{L}} = \frac{1}{3}\int_{0}^{\theta_{\mathrm{L}}/T} C_{\mathrm{L}} T^3 \tau_{\mathrm{L}}(x) J_4(x)\,\mathrm{d}x \tag{58}$$

with

$$i = \mathrm{TO}, \mathrm{TU}, \mathrm{L}; \quad \theta_i = \frac{\hbar\omega_i}{k_{\mathrm{B}}}; \quad C_i = \left(\frac{k_{\mathrm{B}}}{2\pi^2 v_i}\right)\left(\frac{k_{\mathrm{B}}}{\hbar}\right)^3$$

where subscripts TO, TU, and L denote the low-frequency transverse, high-frequency transverse, and longitudinal polarizations of the phonons, respectively, θ_i are the temperature limits corresponding to the cut-off frequencies of the different phonon modes and τ_i are the different scattering mechanisms given as:

$$\tau_{\mathrm{TO}}^{-1} = \begin{cases} B_{\mathrm{T}}\omega T^4 + \dfrac{v_{\mathrm{s}}}{d_{\mathrm{g}}(z=L)}\left(\dfrac{1-p(\omega)}{1+p(\omega)}\right) + A\omega^4, & \text{for P-type dopant} \\ B_{\mathrm{T}}\omega T^4 + \dfrac{v_{\mathrm{s}}}{d_{\mathrm{g}}(z=L)}\left(\dfrac{1-p(\omega)}{1+p(\omega)}\right) + A\omega^4 + \\ \quad \dfrac{2v_{\mathrm{s}}}{\pi d_{\mathrm{g}}(z)}\left(1+\left(\mathrm{e}^{\left(\frac{\pi}{2}\right)^2\Gamma(\omega,\,z)}-1\right)^{-1}\right)^{-1}, & \text{for N-type dopant} \end{cases} \tag{59}$$

$$\tau_{\mathrm{TU}}^{-1} = \begin{cases} \dfrac{B_{\mathrm{TU}}\omega^2}{\sinh(x_\omega)} + \dfrac{v_{\mathrm{s}}}{d_{\mathrm{g}}(z=L)}\left(\dfrac{1-p(\omega)}{1+p(\omega)}\right) + A\omega^4, & \text{for P-type dopant} \\ \dfrac{B_{\mathrm{TU}}\omega^2}{\sinh(x_\omega)} + \dfrac{v_{\mathrm{s}}}{d_{\mathrm{g}}(z=L)}\left(\dfrac{1-p(\omega)}{1+p(\omega)}\right) + A\omega^4 + \\ \quad \dfrac{2v_{\mathrm{s}}}{\pi d_{\mathrm{g}}(z)}\left(1+\left(\mathrm{e}^{\left(\frac{\pi}{2}\right)^2\Gamma(\omega,\,z)}-1\right)^{-1}\right)^{-1}, & \text{for N-type dopant} \end{cases} \tag{60}$$

$$\tau_{\mathrm{L}}^{-1}=\begin{cases} B_{\mathrm{L}}\omega^2T^3+\dfrac{v_{\mathrm{s}}}{d_{\mathrm{g}}(z=L)}\left(\dfrac{1-p(\omega)}{1+p(\omega)}\right)+A\omega^4, & \text{for P-type dopant} \\ B_{\mathrm{L}}\omega^2T^3+\dfrac{v_{\mathrm{s}}}{d_{\mathrm{g}}(z=L)}\left(\dfrac{1-p(\omega)}{1+p(\omega)}\right)+A\omega^4+ & \\ \quad \dfrac{2v_{\mathrm{s}}}{\pi d_{\mathrm{g}}(z)}\left(1+\left(\mathrm{e}^{\left(\frac{\pi}{2}\right)^2\Gamma(\omega,\,z)}-1\right)^{-1}\right)^{-1}, & \text{for N-type dopant} \end{cases} \tag{61}$$

with

$$\frac{1}{v_{\mathrm{s}}}=\frac{1}{3}\left(\frac{2}{v_{\mathrm{TO}}}+\frac{1}{v_{\mathrm{L}}}\right);\quad p(\omega)=\mathrm{e}^{-\pi\left(\frac{2\eta\omega}{v_{\mathrm{s}}}\right)^2};\quad \Gamma(\omega,z)=\sigma_{\mathrm{s}}(\omega)N_{\mathrm{GB}}(z);$$

$$\sigma_{\mathrm{s}}(\omega)=\frac{V_{\mathrm{o}}^2\omega^4}{4\pi v^4};\quad N_{\mathrm{GB}}(z)=\frac{n}{B_{\mathrm{v}}}=\frac{2nd_{\mathrm{g}}(z)}{\pi};\quad A=\frac{nV_{\mathrm{o}}^2}{4\pi v_{\mathrm{s}}^3}\left(\frac{\Delta M}{M}\right)^2;$$

$$V_{\mathrm{o}}=\frac{a^3}{8}$$

where the first terms in equations (59)-(61) are associated with U- and N-processes with constants B_{T} with units K^{-4}, B_{TU} with units s, B_{L} with units $\mathrm{s\,K}^{-3}$, and ω is the phonon angular frequency. The second terms are associated with the boundary scattering with constants v_{s} which is the average phonon velocity, v_{TO} the velocity of the low-frequency transverse phonons, v_{L} the velocity of the longitudinal phonons, $d_{\mathrm{g}}(z)$ the sample characteristic grain dimension in the thickness z and it is estimated from the average distance between the intersections of grain boundaries with a straight line drawn on a top-view electron micrograph of the film layer (Graebner *et al.*, 1994), η the root-mean-squared surface roughness, and the interpretation of $p(\omega)$ is the probability of transmission of a phonon through a grain boundary. Note that scattering is diffusive for $\omega \gg v_{\mathrm{s}}/2\eta$ and specular for $\omega \ll v_{\mathrm{s}}/2\eta$ (Graebner *et al.*, 1994). The third terms are associated with the scattering due to defects or impurities with constant A which is related to the number of impurities in the sample, n is the dopant concentration, V_{o} the atomic volume defined as the atomic weight divided by the density (note that this form of the atomic volume is valid for diamond crystal structures), M is the host atom's atomic mass, and ΔM is the difference between the host and impurity atomic masses. It is worth noting that there appears to exist different definitions for V_{o}. While the original work by Klemens (1955) defines V_{o} as the atomic volume, other researchers such as McConnell *et al.* (2001) define it to be *the crystal lattice volume of the host atom* which suggests the form of $V_{\mathrm{o}}=(4\pi R^3)/3$ where R is the radius of the host atom or $V_{\mathrm{o}}=a^3$. However, note that although A is defined above, *it is still*

a fitting parameter since the number of defects in a layer are dependent on the growth parameters of the film and are not easily obtained from an experiment. Hence, it appears that the actual definition of V_o is unimportant. Impurities in dielectric samples can be of the P-type (e.g. boron) or of the N-type (e.g. phosphorus). Considering that phonon defect scattering is strongly influenced by the grain structure of the material and because only the N-type dopants tend to segregate at the grain boundaries, in addition to the grain boundary scattering the fraction of N-type dopants that are segregated to the grain boundaries are modeled as the fourth term (Goodson, 1996) with constant thickness z, Γ the dimensionless grain-boundary scattering strength (Goodson *et al.*, 1995), N_{GB} is the number density of imperfections per unit grain boundary area, σ_s is the scattering cross-sections of the imperfections, n is the dopant concentration, B_v is the grain boundary area per unit volume which is provided for columnar grain (McConnell *et al.*, 2001).

Holland's model has been extensively, and in good agreement, used to characterize experimental results of single- and polycrystalline silicon thin films by Professor Goodson's group at Stanford University (Asheghi *et al.*, 1998; Goodson, 1996; McConnell *et al.*, 2001). Results of the temperature-dependent thermal conductivity for several Si thin films using the Holland's model are presented later in this paper.

In synthetic diamond films, natural type-IIa, type-Ia diamond and Ge crystals, the N-process scattering rates are largely unknown and the Debye model, which ignores the N-processes, under predicts the strength to which phonons are scattered (Asen-Palmer *et al.*, 1997; Olson *et al.*, 1993). Therefore, a better model to be used is a modified Callaway/Holland model (Asen-Palmer *et al.*, 1997), which includes all phonon polarizations and assumes that the N-processes dominate the scattering and the total thermal conductivity can be expressed as a sum of K_1 and K_2

$$K_1 = HT^3 \sum_{i=1}^{3} v_i^{-1} \int_0^{\theta_i/T} J_4(x) \tau_c^i \, dx \tag{62}$$

$$K_2 = HT^3 \sum_{i=1}^{3} \frac{v_i^{-1} \left(\int_0^{\theta_i/T} J_4(x) \tau_c^i (\tau_N)^{-1} \, dx \right)^2}{\int_0^{\theta_i/T} J_4(x) \tau_c^i (\tau_N \tau_R^i)^{-1} \, dx} \tag{63}$$

with

$$H = \frac{k_B^4}{6\pi^2 \hbar^3}; \quad \theta_i = \left(\frac{6\pi^2}{V_o} \right)^{1/3} \frac{\hbar v_i}{k_B}; \quad \frac{1}{\tau_c} = \frac{1}{\tau_N} + \frac{1}{(\tau_R^i)}$$

where i is associated with the three phonon polarizations, τ_c^{-1} is the combined relaxation rate of the normal (N) and all resistive (R) scattering rates, and V_o is

the atomic volume. Note that K_1 is the Debye model and K_2 is the addition of the thermal resistivity when N-processes are assumed to dominate the scattering (Berman, 1992).

The resistive scatterings are given by (Graebner *et al.*, 1994)

$$\tau_{R,i}^{-1} = A_{u,i} x_\omega^2 T^3 \, e^{\frac{-B_u}{T}} + \frac{v_s}{d_g(z=L)} \left(\frac{1 - p(\omega)}{1 + p(\omega)} \right) + A\omega^4 + \frac{S}{2\pi} \omega + \begin{cases} \dfrac{\pi c_e F^6}{4 v_s^3} \omega^4, & \text{for } \omega < \dfrac{v_s}{F} \\ \dfrac{\pi c_e F^2 v_s}{4}, & \text{for } \omega > \dfrac{v_s}{F} \end{cases} \tag{64}$$

with

$$A_{u,i} = \frac{B k_B^2}{4\pi^2 v_i \hbar^2}; \quad x = \frac{\hbar\omega}{k_B T}; \quad \frac{1}{v_s} = \frac{1}{3}\left(\frac{2}{v_{TO}} + \frac{1}{v_L} \right); \quad A = \frac{n V_o}{4\pi v_s^3} \left(\frac{\Delta M}{M} \right)^2;$$

$$V_o = \frac{a^3}{8}$$

where the first term in equation (64) is associated with the U-processes with constants $A_{u,i}$ with units $s^{-1}K^{-3}$, x is the dimensionless phonon angular frequency, T the temperature, B_u with units K, B with units mK^{-1}, v_i are the phonon velocities corresponding to the low-frequency, high-frequency and longitudinal phonon modes, $\hbar$ is Planck's constant divided by 2π (1.05459×10^{-34} J s), k_B is the Boltzmann constant (1.3807×10^{-23} J/K). The second term is the grain boundary scattering as described earlier. The third term is associated with the scatterings due to defects or impurities. It is important to mention that the definition of A is slightly different from that of Si cases and seems to be more appropriate for use with single-crystal diamond films (Graebner *et al.*, 1994). The fourth term is associated with scattering from strain fields with constant S based on the density of dislocations per unit area. The fifth term is associated with extended defect scattering with constants c_e as the concentration of dopant atoms in m^{-3} and F the diameter of the dopant atom. The scattering due to the N-processes is given by (Graebner *et al.*, 1994)

$$\tau_N^{-1} = A_n x_\omega T^4 \tag{65}$$

where $A_n = C k_B / 2\pi\hbar$, C is a constant with units of K^{-3}

Unphysical scattering accountability. At high temperatures it is possible that some of the resistive scattering mechanisms described earlier lead to non-physical small mean free paths. To eliminate such problem, one can require that (Graebner *et al.*, 1994)

$$\tau_{\mathrm{R}}^{-1} = \left(\frac{\lambda_{\min}}{v_{\mathrm{s}}} + \sum_{i} \left(\tau_{\mathrm{R}}^{i} \right)^{-1} \right)^{-1} \tag{66}$$

where $\lambda_{\min}$ is a minimum mean free path and τ_{R}^{i} represents the sum of all the above resistive scattering mechanisms. $\lambda_{\min}$ has been modeled as either the interatomic dimension or half of the wavelength (Graebner *et al.*, 1994).

In addition to the above scattering rates, contributions due to microcracks are introduced by multiplying a temperature-independent constant $M_{\mathrm{c}} \leq 1.0$ to the combined form of equations (62) and (63) (Graebner *et al.*, 1994). This seems to characterize accurately several experimental findings and provide information about the total resistance to the heat flow.

Based on known theory of scattering mechanisms, these methods are being used by Professor Majumdar's group at Berkeley (Majumdar, 1993), Graebner and colleagues at AT&T Bell Laboratories (Graebner *et al.*, 1994), Professor Goodson's group at Stanford (Asheghi *et al.*, 1998; Goodson, 1996; Goodson *et al.*, 1995; McConnell *et al.*, 2001) and Professor Chen's group presently at MIT (Chen, 1997, 1998, 2000) for extracting the total mean free paths λ.

Note that Holland's and the modified Callaway/Holland's models are a solution of the steady-state version of the BTE and can only provide the temperature-dependent results of thermal conductivity and therefore only addresses the issue of microscopic size, i.e. it can only determine thermal conductivity as a function of size. The EPRT appears to be valid in providing the bridging for microscopic time issues (Joshi and Majumdar, 1993) but yields results that are different from that provided by the Cattaneo model. This discrepancy has not been explained to date because of the lack of experimental data for small time scales.

The theory described above is further tested in the "Results and discussion" section based on experimental data obtained for single-crystal silicon films (Asheghi *et al.*, 1998), polycrystalline silicon films (McConnell *et al.*, 2001), and synthetic diamond films (Graebner *et al.*, 1994).

Table IV gives information on the various constants described throughout this section for a few selected materials.

MD

MD is a computer simulation technique where the time evolution of a set of interacting atoms is tracked by integrating their classical equations of motion. This equation corresponds to the second law of classical mechanics formulated by Sir Isaac Newton in 1687

$$\vec{F}_i = m_i \vec{a}_i \tag{67}$$

Constant	Si	Ge	C
v_{TO} (m/s)	5.86×10^{3}[a]	3.55×10^{3}[a]	–
v_{TU} (m/s)	2.0×10^{3}[a]	1.3×10^{3}[a]	–
v_{L} (m/s)	4.24×10^{3}[a]	2.46×10^{3}[a]	–
θ_{TO} (K)	180[a]	101[a]	–
θ_{TU} (K)	210[a]	118[a]	–
θ_{L} (K)	570[a]	333[a]	–
v_{s} (m/s)	5.2×10^{3}	3.1×10^{3}	13,500[b] or 12,288[c]
a (Å)	5.43	5.658	3.567
A_u ($s^{-1}K^{-3}$)	–	–	640[b]
A_n ($s^{-1}K^{-4}$)	–	–	1.499
B_u (K)	–	–	470[b] or 670[d]
B (cm/K)	–	–	1.5×10^{-12}[d]
C (K^{-3})	–	–	7.2×10^{-11}[d]
B_T (K^{-4})	9.3×10^{-13}[a]	1×10^{-11}[a]	–
B_{TU} (s)	5.5×10^{-18}[a]	5.0×10^{-18}[a]	–
B_L (s/K^3)	2.0×10^{-24}[a]	6.9×10^{-24}[a]	–
A (s^3)	$O(10^{-43})$-$O(10^{-46})$	$O(10^{-44})$	$O(10^{-30})$
η (Å)	1-10	–	100
V_o (m^3)	2.0×10^{-29}	2.3×10^{-29}	5.67×10^{-30}
d_g (nm)	0.1-3000		1,000-10,000
S	–	–	43×10^{-5}[d]
F (nm)	–	–	1.5[d]
c_e (m^{-3})	–	–	19×10^{22}[d]
Mc	–	–	0.95[d]

Notes: [a]Holland (1963), [b]Goodson *et al.* (1995), [c]Majumdar (1993), and [d]Graebner *et al.* (1994).

Table IV.
Data used by different researchers in the prediction of the relaxation time of silicon, germanium and diamond

where $\vec{F}$ is the force acting on the atom i at a given time in a system containing N atoms, m_i is the atom mass, and $\vec{a}_i$ is the atom acceleration given by

$$\vec{a}_i = \frac{\mathrm{d}^2\vec{r}_i}{\mathrm{d}t^2}$$

with $\vec{r}_i$ as the atom position.

The force is obtained from the gradient of the interatomic potential energy surface $U(r_1,r_2, \ldots, r_N)$ as a function of the positions of all the atoms:

$$\vec{F}_i = -\vec{\nabla}_{r_i} U(\vec{r}_1, \vec{r}_2, \ldots, \vec{r}_N) \tag{68}$$

where $\vec{\nabla}_{r_i}$ operates on the position r_i of atom i. Any change in the potential energy that results from a displacement of atom i contributes to the force acting on atom i.

After the initial conditions and the interaction potential are defined, the equations of motion are numerically solved (Ercolessi, 1997). The molecular dynamics simulation provides information at the microscopic level via positions and velocities of all atoms as a function of time,

$$\vec{r}_i(t), \vec{v}_i(t).$$

However, the important information that can be obtained from the simulations are the macroscopic properties of the system. This sequence of points that are generated belong to the same ensemble. These describe the state of a system. *An ensemble can be defined as a collection of all possible systems which have different microscopic states but have an identical macroscopic or thermodynamic state* (Stote *et al.*, 1999). These ensembles can be described by thermodynamic states that are kept constant such as the number of atoms (N), volume (V), energy (E), temperature (T), pressure (P) and chemical potential (μ):

- microcanonical ensemble (NVE);
- canonical ensemble (NVT);
- isobaric-isothermal ensemble (NPT); and
- grand canonical ensemble (μVT).

MD can be viewed either as a deterministic or statistical mechanics technique. As a deterministic technique it is given an initial set of positions and velocities and the subsequent time evolutions are completely determined (Ercolessi, 1997). As a statistical mechanics technique, it generates a set of configurations that are distributed according to statistical distribution functions. In cases where thermodynamic parameters are of interest, the MD information can be averaged over all the atoms in the system and over the time of the simulation. In order to achieve these different ensembles the following thermostats can be used (Brenner, 1997).

- Velocity scaling – the wanted temperature is achieved by multiplying each atomic velocity by a scaling factor.
- Langevin – a heat bath is modeled by adding random and frictional forces to the velocity of each particle. The wanted temperature is reached by balancing these two forces.
- Berendsen – the difference between the desired and the current temperature of the system can generate a friction coefficient that heats (if negative) or cools (if positive) each atom in the system.
- Hoover – the system is kept at a constant temperature by adding terms to the interatomic forces which maintain a constant kinetic energy.
- Nose – which adds terms to the forces similar to Hoover, however the terms allow fluctuations in temperature that mimic those that would occur if the simulated systems were part of a macroscopic system.

MD is a computer simulation that often can be considered to be just as good as the experiment (Rapaport, 1995). Therefore, MD is viewed as an important tool for solving the thermal conductivity of very thin films.

The following subsections describe several important issues in acquiring thermodynamic information in the process of running a MD simulation.

Building initial configurations. The different physical properties of solids are closely related to their crystal structures. There are 14 Bravais lattices, and most of the elements found in the periodic table can be depicted by the hexagonal close-packed structure and the three major cubic configurations: simple cubic (sc); body-centered cubic (bcc), and face-centered cubic (fcc).

The Bravais lattice defines a crystalline solid by specifying the periodic array in which the repeated units of a crystal are arranged. These Bravais lattices are defined by three primitive vectors as shown in Figure 5(a). The real crystal structure is composed of the copies of the same physical unit (such as the NaCl shown in Figure 5(b), called basis, which are located at the points of a Bravais lattice. Table V provides some information on the different lattices with basis.

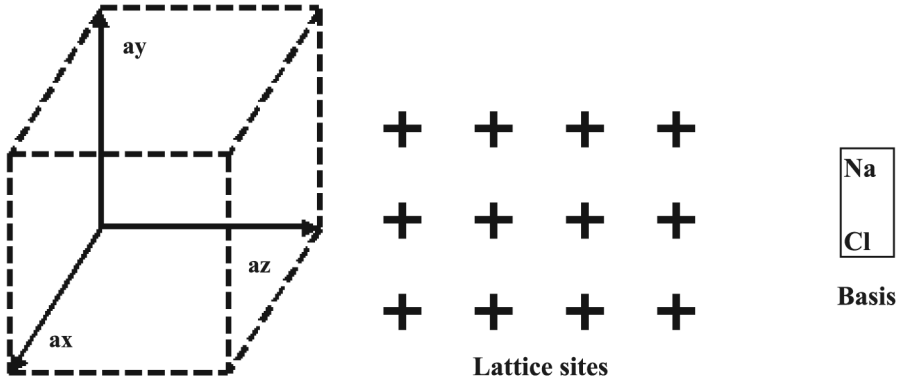

(a) Representation of the primitive vectors of a unit cell

(b) Representation of Bravais lattice sites and basis

Figure 5.
Representation of primitive unit vectors and basis of a Bravais lattice

	SC	BCC	FCC	Diamond
Unit cell volume	a^3	a^3	a^3	a^3
Lattice points per cell	1	2	4	8
Location of basis	0	0	0	0
		$a/2\,(\hat{x}+\hat{y}+\hat{z})$	$a/2\,(\hat{x}+\hat{y})$	$a/2\,(\hat{x}+\hat{y})$
			$a/2\,(\hat{y}+\hat{z})$	$a/2\,(\hat{y}+\hat{z})$
			$a/2\,(\hat{x}+\hat{z})$	$a/2\,(\hat{x}+\hat{z})$
				$a/4\,(\hat{x}+\hat{y}+\hat{z})$
				$a/4\,(3\hat{x}+3\hat{y}+\hat{z})$
				$a/4\,(\hat{x}+3\hat{y}+3\hat{z})$
				$a/4\,(3\hat{x}+\hat{y}+3\hat{z})$

Table V.
Basis information

Figure 6 presents the unit cell of a diamond and zincblende structure for illustration. The lattice sites shown correspond to carbon atoms covalently bonded to four nearest neighbors. This structure is obtained from superimposing two fcc Bravais lattices displaced from each other by one-quarter of a unit cell. Figure 7 is a computer generated diamond crystal structure. Two other elements in the periodic table form the diamond structure: silicon and germanium. When instead of carbon atoms, the lattice sites are replaced by zinc and sulfur atoms, or gallium and arsenide, GaAs (semiconducting compounds from the Groups III and IV), the diamond structure is called a zincblende structure (Hook and Hall, 1991).

Carbon nanotubes (CNTs) were discovered in the early 1990s (Iijima, 1991; Iijima and Ichihashi, 1993; Thess *et al.*, 1996) and possess unique thermal,

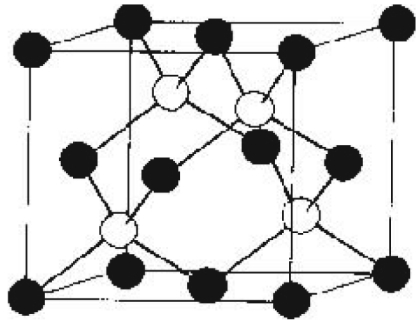

Source: Hook and Hall (1991)

Figure 6.
The diamond and zincblende structure. The diamond structure is formed from carbon atoms occupying all lattice spaces and the zincblende is formed from zinc and sulfur atoms occupying the lattice spaces

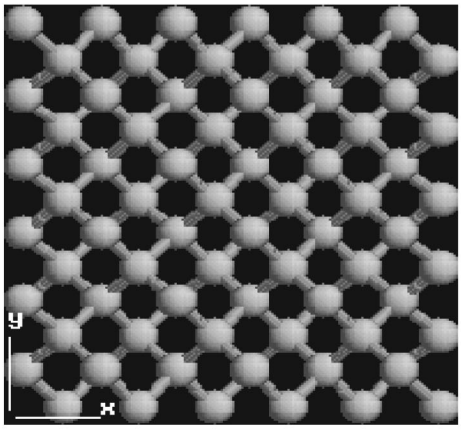

(a) Representation of the cross sectional area (x- and y-directions) through which heat is applied in a diamond structure

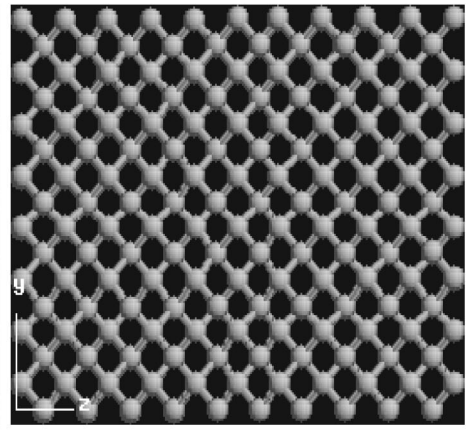

(b) Representation of the z-direction which heat flows in a diamond film structure

Figure 7.
Representation of a diamond structure constructed $3 \times 3 \times 5$ cells along the *x*-, *y*-, and *z*-directions

mechanical and electronic properties. Two classes of CNTs were observed. Single-wall carbon nanotubes (SWNTs) are composed of hexagonal lattices similar to a single sheet of graphite, which is rolled-up to form a tube with typical diameters of 1-20 nm. Multi-wall carbon nanotubes (MWNTs) are two or more SWNTs concentrically arranged like the ripples formed in water.

SWNTs or MWNTs are of different types based on a pair of integers (n, m), which denotes the chirality of the tube: armchair ($n = m$), zigzag ($n = 0$ or $m = 0$), and chiral (or helical for any other combination of n and m) (Figure 8). All armchair tubes are metallic, the conduction bands are shown to cross the Fermi level (Wildöer *et al.*, 1998). Zigzag and chiral tubes are observed to behave in two ways: if $n - m = 3k$ (and k is an integer), these tubes are metallic and if $n - m \neq 3k$, the tubes are semiconducting with a small (~ 0.5 eV) band gap which is inversely dependent on the tube diameter (Wildöer *et al.*, 1998).

The reader is referred to Saito *et al.* (1992) and Wildöer *et al.* (1998) for more in-depth examination of the construction of nanotubes. Figure 9 provides an example of a (10, 10) nanotube.

Boundary conditions. The MD computational cell, used to study real systems, contains several hundreds to a few thousand atoms. This system is much smaller than the real system and in order to certify that the size limitation of the computational cell does not introduce errors to the simulation results, the boundary conditions must be chosen carefully.

- *Free boundaries*. This is a case where no boundaries are assigned to the system. The molecules are free to move within the system. This works well for cases where particles are in a vacuum. It is appropriate for ultrafast processes when the effect of the boundaries are unimportant due to the short time scales of the involved process.

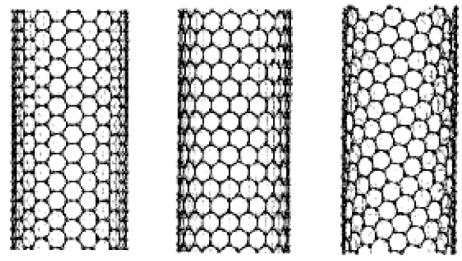

Note: The armchair nanotube has $m = n$ which leads to the common "_/‾_/" shape, the zigzag nanotube has $m = 0$ which leads to the common "⋀⋀" shape in the direction perpendicular to the tube axis and the chiral nanotube is any combination of n and m in the direction perpendicular to the tube axis

Source: Iijima (2002)

Figure 8.

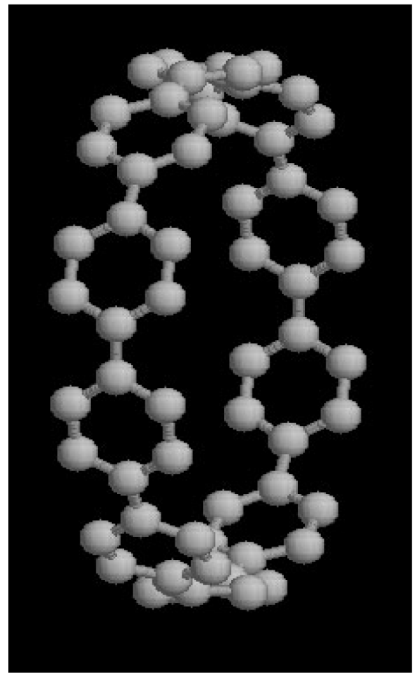

Figure 9.
Section of a (10, 10) nanotube with 60 atoms

- *Rigid boundaries*. This is a case where the atoms at the boundaries are fixed. This is an unphysical situation, which is introduced to study boundary effects.
- *Periodic boundaries*. This is the most popular choice of boundary conditions and is used mainly to eliminate the surfaces. Periodic boundary conditions are in essence similar to the explanation of Bravais lattices where a copy of a computational cell is replicated in space infinitely (Figure 10).
- *Mixed boundaries*. This is any combination of the above boundary conditions where the system can be set to be periodic in one or two directions and free or rigid in the other directions.

Interatomic potentials. The model for the physical system comes from choosing the potential. This is a function of the positions of the nuclei, representing the potential energy of the system when the atoms are arranged at specific positions. The well-established and understood pair potential such as the Lennard-Jones (6-12) potential is not useful for elements that form diamond-like structures such as Si, C, and Ge. This is true for all semiconductors and other covalently-bonded systems. The Stillinger-Weber Potential (SWP) (Stillinger and Weber, 1985) is one of the first potentials introduced for modeling a

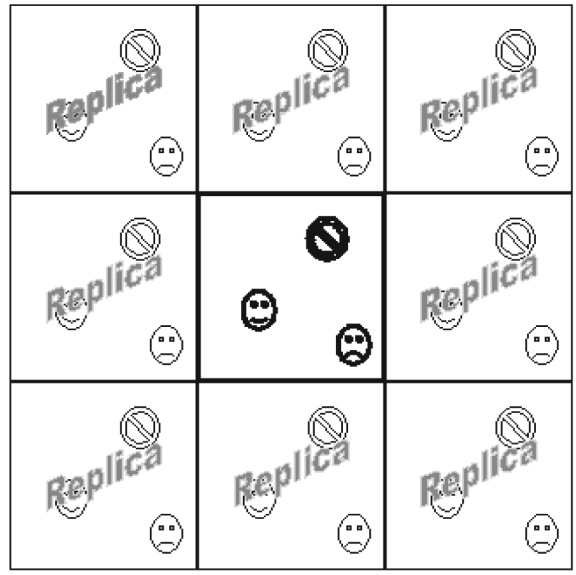

Figure 10.
Replica of computational cell used for periodic boundary conditions

semiconductor using a classical model. The main advantage in using the SWP is its simplicity. However, it has a built-in diamond-like tetrahedral structure, which hinders transferability (Ercolessi, 1997). Tersoff (1988a, b) proposed a family of many-body potential functions, which are based on the bond order concept that depends on the local environment (i.e. its nearest neighbors). This eliminates the *transferability problem* by allowing a potential that can study silicon, germanium, carbon and a combination of these atoms (Maruyama, 2000). The Tersoff-Brenner potential (Brenner, 1990) is a modified version of Tersoff's potential to include the hydrocarbon system, which is widely used with CNTs. The reader is referred to Chapter 6 in Maruyama (2000) for a unified representation of the Tersoff and Brenner's potentials. For simplicity, only the Stillinger and Webber potential is described here.

The Stillinger-Weber potential (Stillinger and Weber, 1985). The many-body total potential energy of the system of N atoms interacting is:

$$U(\vec{r}_1, \vec{r}_2, \ldots, \vec{r}_{\mathrm{N}}) = \sum_i \sum_{j>i} U_{i,j}^{(2)} + \sum_i \sum_{j>i} \sum_{k>j} U_{i,j,k}^{(3)} \tag{69}$$

where $\vec{r}$ are the positions of the atoms, $U_{i,j}^{(2)}$ is the two-body term and $U_{i,j,k}^{(3)}$ is the three-body term contribution to the total potential U. The two-body term is

$$U_{i,j}^{(2)} = \varepsilon A \left(B \left(\frac{r_{ij}}{\sigma} \right)^{-p} - 1 \right) \mathrm{e}^{\left(\frac{1}{r_{ij}/\sigma - a} \right)} \tag{70}$$

and the three-body term is

$$U_{i,j,k}^{(3)} = \varepsilon\lambda e^{\left(\frac{\gamma}{r_{ij}/\sigma - a} + \frac{\gamma}{r_{ik}/\sigma - a}\right)} \left(\cos(\theta_{ijk}) + \frac{1}{3}\right)^2 \quad (71)$$

where $r_{ij} = |\vec{r}_i - \vec{r}_j| = \sqrt{(x_i - x_j)^2 + (y_i - y_j)^2 + (z_i - z_j)^2}$, the cut-off of this potential is determined by $r_c = \sigma a$, θ_{ijk} is the angle centered on atom i and is given by $\cos\theta_{ijk} = \vec{r}_j \cdot \vec{r}_k / (r_j r_k)$, and ε, λ, σ, γ, A, B, p, and a are parameters of the Si crystal structure provided in Table VI.

Integration algorithms of the equation of motion (EOM). The basic idea for all time integration algorithms of the EOM is to advance the system variables through a discrete step in time by approximating the action of the derivative via finite differences. In MD, typical Runge-Kutta schemes are not used because they are time-consuming. It would be necessary to solve four force evaluations per atom per step (Haile, 1992). The common criteria for the different time integrators are that it should:

- minimize the need for the force calculation;
- be stable;
- be accurate;
- adhere to conservation of momentum and energy for the whole system; and
- possibly be time-reversible.

The most popular integration algorithms used for MD simulations are the:

(1) Verlet;
(2) leap-frog;
(3) velocity Verlet; and
(4) predictor-corrector
    - Nordsieck
    - gear.

The most commonly used time integration algorithm (Ercolessi, 1997) is the Verlet algorithm and it is further described below.

Verlet algorithm The simplest finite-difference method used in MD is a third-order Störner algorithm first used by Verlet. This method uses the combination of two Taylor expansions. First we define the Taylor series for position from t to $t + \delta t$

ε (eV)	γ	σ (Å)	a	λ	A	B	p
2.16826	1.20	2.0951	1.8	21	7.049556277	0.6022245584	4

Source: Stillinger and Weber, (1985)

Table VI. Parameters used for silicon in the SWP

$$x(t+\delta t) = x(t) + \frac{\mathrm{d}x(t)}{\mathrm{d}t}\delta t + \frac{1}{2}\frac{\mathrm{d}x^2(t)}{\mathrm{d}t^2}\delta t^2 + \frac{1}{3}\frac{\mathrm{d}x^3(t)}{\mathrm{d}t^3}\delta t^3 + \mathrm{O}(\delta t^4) \tag{72}$$

and t to $t-\delta t$

$$x(t-\delta t) = x(t) - \frac{\mathrm{d}x(t)}{\mathrm{d}t}\delta t + \frac{1}{2}\frac{\mathrm{d}x^2(t)}{\mathrm{d}t^2}\delta t^2 - \frac{1}{3}\frac{\mathrm{d}x^3(t)}{\mathrm{d}t^3}\delta t^3 + \mathrm{O}(\delta t^4) \tag{73}$$

By adding equations (72) and (73)

$$x(t+\delta t) = 2x(t) - x(t-\delta t) + \frac{\mathrm{d}x^2(t)}{\mathrm{d}t^2}\delta t^2 + \mathrm{O}(\delta t^4) \tag{74}$$

Generally,

$$r(t+\delta t) = 2r(t) - r(t-\delta t) + a(t)\delta t^2 + \mathrm{O}(\delta t^4) \tag{75}$$

where $a(t)$ is the force divided by the mass. The Verlet algorithm uses the positions and accelerations at time t and the positions from time $t-\delta t$ to calculate the new positions at time $t+\delta t$. Its advantages are that it is fairly straightforward and the storage requirements are small. The disadvantages are that the velocities are not directly generated and it is of moderate precision.

Physical properties. The following discusses the most common physical properties that are obtained from the MD simulation.

Potential energy. The total many-body potential is given by (Evans and Morriss, 1990)

$$U(\vec{r}_1, \vec{r}_2, \ldots, \vec{r}_{\mathrm{N}}, t) = \sum U_i + \frac{1}{2!}\sum \overset{(2)}{U}_{i,j} + \frac{1}{3!}\sum \overset{(3)}{U}_{i,j,k} + \cdots \tag{76}$$

where the total potential energy is resolved by the interactions of N identical particles into one-body U_i, two-body $U^{(2)}_{i,j}$, three-body $U^{(3)}_{i,j,k}$, etc. contributions.

Kinetic energy. The average kinetic energy is given by

$$\mathrm{KE}(t) = \frac{1}{2}\sum_{i}^{N} m_i(v_i(t))^2 \tag{77}$$

where N is the total number of atoms, and $m_i v_i$ denotes the molecular moment via the atom's masses (m) and velocities (v).

Total energy. The total energy of the system is given by

$$E = U + \mathrm{KE} \tag{78}$$

which is the sum of the potential (U) and kinetic (KE) energies. Note that although both potential and kinetic energies are subject to fluctuations, the total energy must be preserved (Haile, 1992).

Temperature. The instantaneous temperature is given by the kinetic temperature

$$\mathrm{KE}(t) = \frac{3}{2} N k_{\mathrm{B}} T \tag{79}$$

where k_{B} is the Boltzmann constant.

Thermal conductivity: direct method. The direct method is a nonequilibrium molecular dynamics (NEMD) computer simulation that is analogous to an experimental situation in which a temperature gradient across the simulation cell is applied. To simulate heat flow from a hot to cold region, the specimen is divided into M equal segments perpendicular to the z direction. For periodic boundary conditions the slabs are created as shown in Figure 11(a) and for rigid boundary conditions the slabs are created as shown in Figure 11(b).

The instantaneous temperature T_i in a slab i is determined from the kinetic energies of the N_i atoms within that slab

$$T_i = \frac{1}{3 N_i k_{\mathrm{B}}} \sum_{k}^{N_i} m_k v_k^2 \tag{80}$$

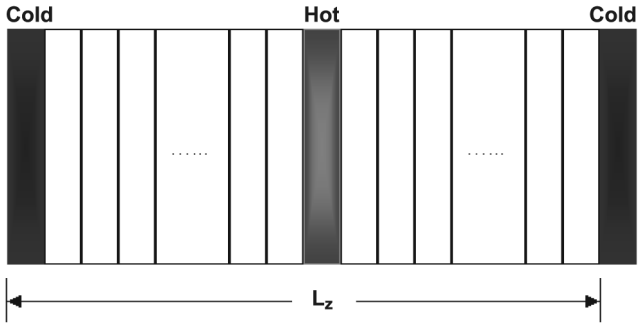

(a) Slabs for periodic boundary configurations

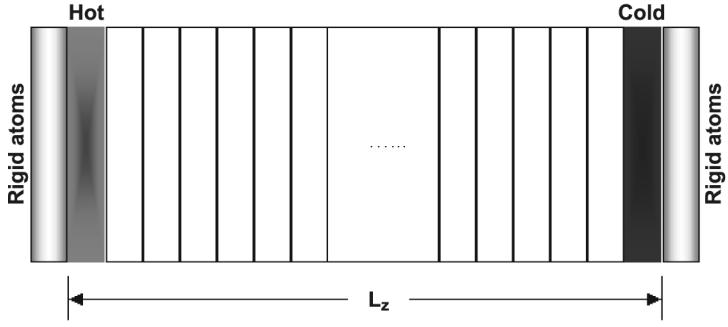

(b) Slabs for rigid boundary configurations

Figure 11.
Slabs in MD

where the masses m_k and velocities v_k are of atoms k in the slab i and k_B is the Boltzmann constant. The temperature profile is then calculated by time averaging (Muller-Plathe, 1997).

The temperature and its gradient are averages calculated over time as well as over many particles, so they are better defined and should converge rapidly (Muller-Plathe, 1997). The atoms in the boundary slab interact with the atoms in the rest of the specimen and at equilibrium a thermal flux is maintained via energy exchange between the hot and cold regions. The heat flux in a given direction in a thermally equilibrated slab is calculated according to

$$q = \frac{\left\langle \frac{1}{2}\sum_{k=1}^{N_B} m_k\left(v_k'^2 - v_k^2\right)\right\rangle}{A\Delta t} \tag{81}$$

where A is the cross-sectional area, Δt is the time step taken to be 0.5 fs, and N_B is the number of atoms in the boundary layer. v_k and v_k' are the velocities of the atoms in the hot and cold slabs before and after scaling, respectively (Osman and Srivastava, 2001).

Figure 11(a) depicts the configuration of the system for periodic boundary conditions and can be extended for crystal structures in three dimensions or for nanotubes in an uniaxial dimension. The first slab on the left is set to a cold temperature and the hot temperature is set to a slab in the middle of the specimen $(N/2 + 1)$. This is to allow the usage of periodic boundary conditions as described by Muller-Plathe (1997). For crystal structures, bulk properties are studied by setting all three directions to be periodic, while the nanotube will only have periodic conditions set perpendicular to the tube axis. Note that this periodic arrangement will double the area available for the heat to flow (energy can flow in two directions from the hot slab).

In Figure 11(b), the first and last slabs consist of rigid atoms which duplicate the case of actual boundaries allowing for boundary scattering by the particles within the system. The cold and hot slabs are set to the slabs immediately adjacent to the rigid atoms. The heat flux is calculated similar to equation (81). In the study of thin films, the structure shown in Figure 11(b) is slightly modified to include all three directions; while the z-direction is kept to include the rigid atoms, the x- and y-directions are set to be periodic (Lukes *et al.*, 2000; Schelling *et al.*, 2002).

Finally, the thermal conductivity is calculated based on Fourier law

$$K = -\frac{q}{\left\langle \frac{dT}{dz}\right\rangle} \tag{82}$$

where dT/dz is the gradient of the temperature T which is the only unknown obtained as an ensemble average (note that in the case of periodic boundary conditions, we obtain two temperature profiles while with the rigid boundary conditions only one profile is obtained).

The heat current flows in a well-defined direction in the lattice, the simulation will only provide K in one crystal lattice direction. To obtain K in the other lattice directions, an entirely new simulation must be performed. Note that this is inherent of the direct method only. When an equilibrium molecular dynamics (EMD) simulation is performed such as the Green-Kubo method (Che *et al.*, 2000; Schelling *et al.*, 2002; Volz and Chen, 1999), the entire thermal conductivity tensor is computed in just one simulation (Schelling *et al.*, 2002). However, note that the direct method simulates an experiment directly, so it is a much simpler method to compute the thermal conductivity and the Green-Kubo method also presents other limitations that are eliminated in the direct method (Schelling *et al.*, 2002).

Results and discussion

Results based on the Holland model

Figure 12 shows the temperature-dependent data for several experiments conducted on several film thicknesses of doped and undoped single- and polycrystalline silicon films. These data are used for comparison with the theories developed earlier. Note that the theories developed earlier have been used to explain partially these experimental results in the work by

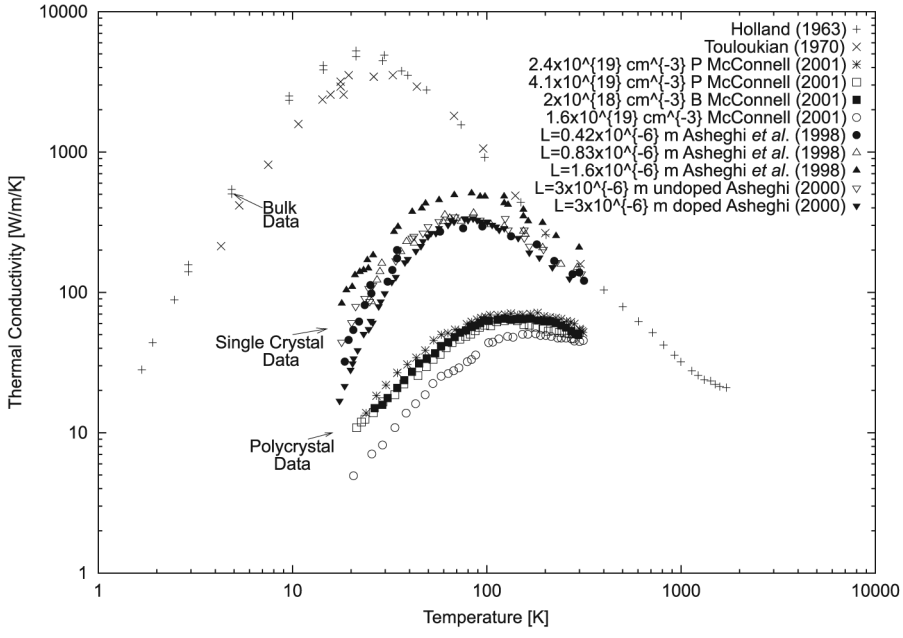

Figure 12.
Experimental thermal conductivity data for several silicon films according to temperature

Note: Data for bulk materials is for single-crystal film (Holland, 1963), data for single-crystal thin films is obtained from Asheghi (Asheghi *et al.*, 1998), and data for polycrystalline thin films is obtained from McConnell (McConnell *et al.*, 2001)

McConnell *et al.* (2001). However, the results shown here differ ever so slightly form those reported earlier, and we attempt to provide some insight into the different parameters that were used to fit these data.

The results presented in Figure 13 are based on the experimental data and the theoretical fit in the work provided by Holland (1963). The best fit approximation for bulk single-crystal silicon and germanium samples were obtained in this study by using equation (55) with the defect scattering parameters $A_{Si} = 1.32 \times 10^{-45}\,s^3$ and $A_{Ge} = 2.4 \times 10^{-44}\,s^3$, respectively. However, the reported defect scattering parameter for silicon provided by Holland (1963) is one order of magnitude greater than that found in this study, $A_{Si} = 1.32 \times 10^{-44}\,s^3$. This suggests that the reported value by Holland could be in error considering that the same theory is used and the parameter for Ge matches the parameter in Holland's work.

As in the work by McConnell *et al.* (2001), the results presented in Figures 14(a)-16(b) are based on Holland's method (equation (55)) and assume that the scattering mechanisms present for both doped and undoped samples are U- and N-processes, grain boundaries, and defects. The fitting parameters for all cases are the defect scattering parameter A, the rms grain boundary surface roughness η, and the maximum grain size $d_g(z = L)$. These parameters are contrasted and summarized in Table VII.

The chosen parameters that provide the best fit to the undoped data in Figure 14(a) are the defect scattering parameter $A = 1.32 \times 10^{-45}\,s^3$, the rms

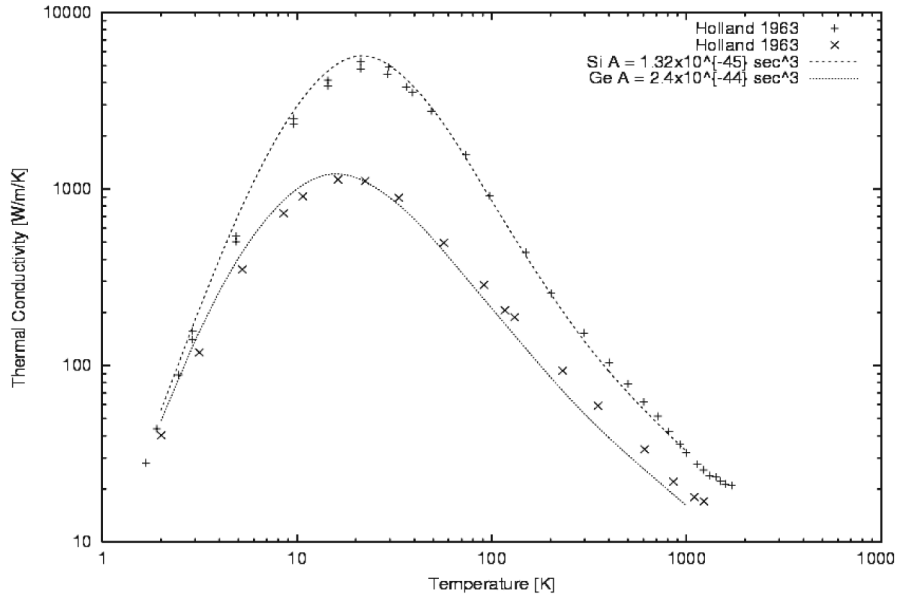

Figure 13.
The best fit of temperature-dependent thermal conductivity for the experimental thermal conductivity data of silicon and germanium samples following theory presented by Holland

Source: Holland (1963)

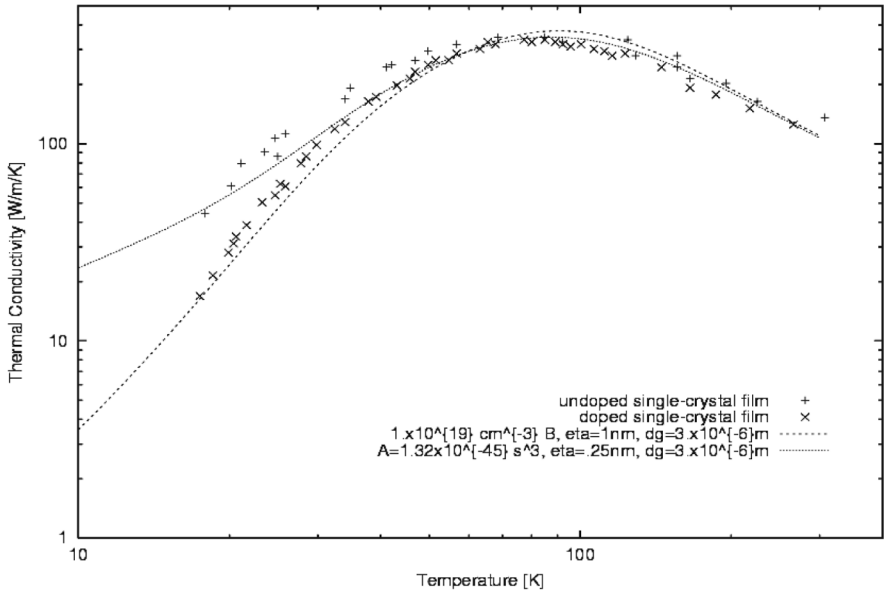

(a) Comparison of temperature-dependent thermal conductivity data and predictions following the theory in Section

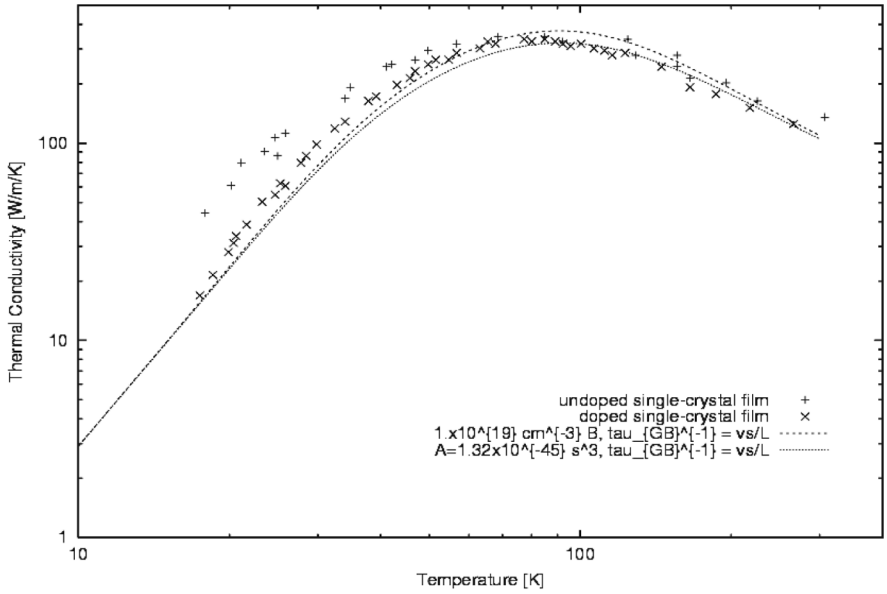

(b) Comparison of temperature-dependent thermal conductivity data and predictions following the theory in Section

Source: McConnell (2001)

Figure 14.
Comparison of thermal conductivity of single-crystal doped and undoped silicon films of thickness $L = 3\ \mu$m

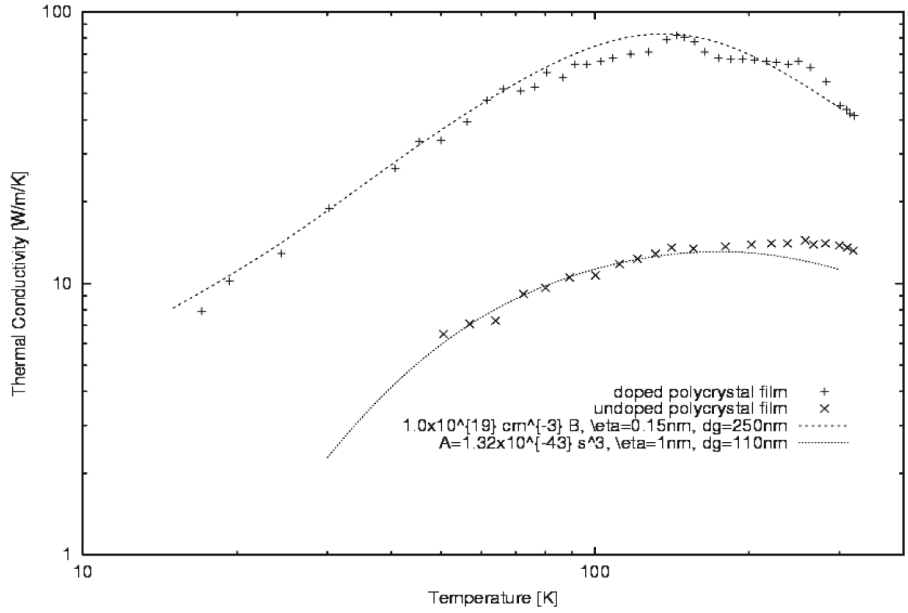

Figure 15.
Comparison of thermal conductivity of doped and undoped polycrystalline silicon films of thickness $L = 1\,\mu$m

Source: McConnell *et al.* (2000)

grain boundary surface roughness $\eta = 0.25\,$nm, and the maximum grain size $d_g(z = L) = 3\,\mu$m. It is interesting to point out that the value for the defect scattering parameter is of the same order of magnitude as the one used to obtain the best fit of the experimental data of bulk single-crystal provided by Holland (1963). This indicates that the relative number of defects in the undoped single-crystal film is comparable to the defects found in the bulk single-crystal material. The chosen parameters that provide the best fit of the doped data in Figure 14(a) are the defect scattering parameter $A = 4.38 \times 10^{-46}\,\mathrm{s}^3$, the rms grain boundary surface roughness $\eta = 1\,$nm, and the maximum grain size $d_g(z = L) = 3\,\mu$m. The value for the defect scattering parameter is obtained from the A equation (equation (59)) and is based on the boron-dopant concentration of $n = 1.0 \times 10^{19}\,\mathrm{cm}^{-3}$ as provided in the experiment conducted by Asheghi (McConnell *et al.*, 2001).

The results shown in Figure 14(b) are similar to the results shown in Figure 14(a) with the exception that the term v_s/L is added to equations (59)-(61). This is suggested by Graebner *et al.* (1994) for small samples. Note that although this version of the grain boundary equation recovers the overall behavior of the temperature-dependent thermal conductivity for temperatures higher than 70 K, it cannot recover the correct behavior at the lower temperatures.

From the theory described earlier in contrast to past efforts and interpretations, the fitting provided in Figure 14(a) suggests that a better

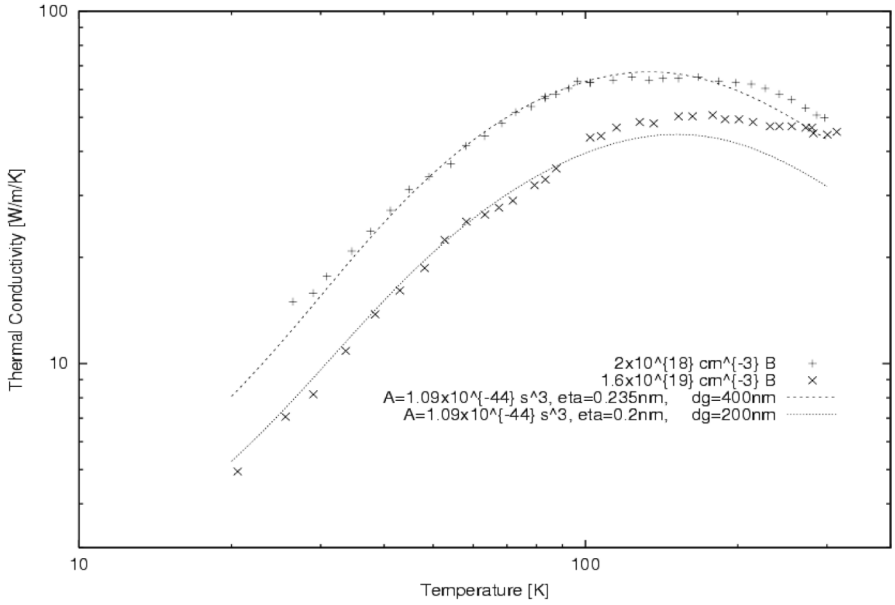

(a) Comparison of temperature-dependent thermal conductivity data and predictions following the theory in Section

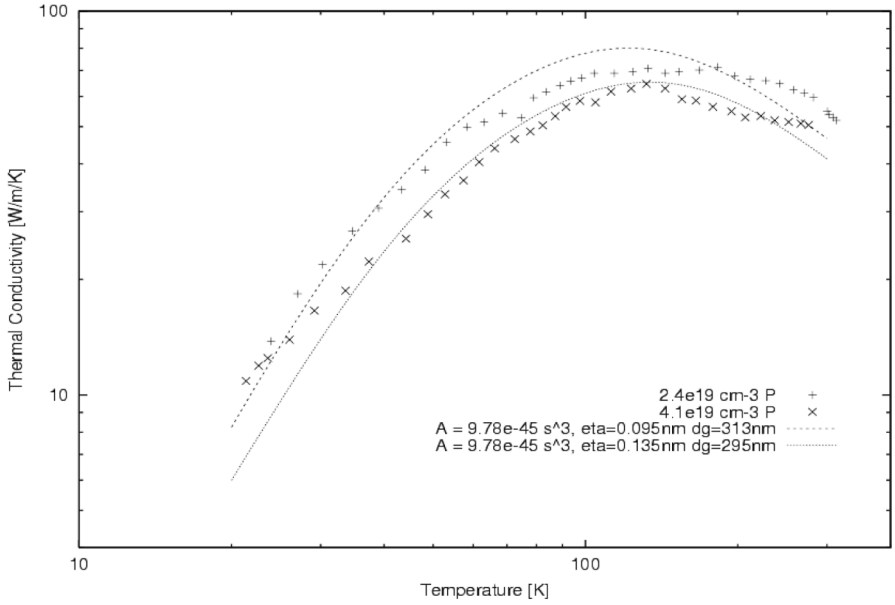

(b) Comparison of temperature-dependent thermal conductivity data and predictions following the theory in Section

Source: McConnell *et al*. (2001)

Figure 16.
Comparison of thermal conductivity of polycrystalline silicon films of thickness $L = 1\,\mu$m

	Sample	η(nm)	d_g	$n(\mathrm{cm}^{-3})$	$A(\mathrm{s}^3)$
McConnell *et al.* (2000)[a]	usc	–	3 μm	–	–
Present work (Figure 14(a))	usc	0.25	3 μm	–	1.32×10^{-45}
McConnell *et al.* (2000)[a]	Bdsc	–	3 μm	1×10^{19}	–
Present work (Figure 14(a))	Bdsc	1	3 μm	–	4.38×10^{-46}
McConnell *et al.* (2000)	upc	1	190 nm[c], 5 nm[b]	–	1.32×10^{-43}
Present work (Figure 15)	upc	1	110 nm	–	1.32×10^{-43}
McConnell *et al.* (2000)	Bdpc	–	243 nm[c]	1.0×10^{19}	6.932×10^{-44}
Present work (Figure 15)	Bdpc	0.15	250 nm	–	4.38×10^{-46}
McConnell *et al.* (2001)	Bdpc	0.1	400 nm	2.0×10^{18}	1.9×10^{-44}
Present work (Figure 16(a))	Bdpc	0.235	400 nm	25×10^{19}	1.09×10^{-44}
McConnell *et al.* (2001)	Bdpc	0.35	408 nm	1.6×10^{19}	1.0×10^{-44}
Present work (Figure 16(a))	Bdpc	0.2	200 nm	25×10^{19}	1.09×10^{-44}
McConnell *et al.* (2001)	Pdpc	0.1	313 nm	2.4×10^{19}	1.0×10^{-44}
Present work (Figure 16(b))	Pdpc	0.095	313 nm	8.0×10^{19}	9.78×10^{-45}
McConnell *et al.* (2001)	Pdpc	0.135	295 nm	4.1×10^{19}	1.0×10^{-44}
Present work (Figure 16(b))	Pdpc	0.135	295 nm	8.0×10^{21}	9.78×10^{-45}

Table VII.
Parameters used in fitting the Holland model to available experimental data

Note: [a]These results were not fitted in the work of McConnell *et al.* (2000); [b]the reported value is for $d_g(z=0)$; [c]the reported value is for $d_g(z=L)$; usc – undoped single crystal; Bdsc – boron-doped single crystal; upc – undoped polycrystal; Bdpc – boron-doped polycrystal; Pdpc – phosphorus-doped polycrystal.

equation for the grain boundary effect for small doped and undoped single-crystal samples would be a version similar to that of equations (59)-(61) where the term $d_g(z=L)$ be replaced by the film thickness L. In this study, we adopt a slight change in the definition of d_g which must be defined as the characteristic dimension that is parallel (and not perpendicular) to the flow of heat. Also, we find that the rms grain boundary surface roughness η has great impact in controlling the low temperature behavior of the temperature-dependent thermal conductivity of single-crystal films. This distinction is clearly depicted in results of Figure 14.

Figure 15 provides theoretical predictions of the temperature-dependent thermal conductivity using equation (55) and the boron-doped and undoped (McConnell *et al.*, 2000) experimental data of polysilicon films. Because of the columnar structure of polycrystalline films, the maximum grain size $d_g(z=L)$ in the grain boundary equation is the average size of the grains as computed from the average value of the micrograph results (and not the film thickness as proposed by the single-crystal results).

In Figure 15, the parameters that provide the best fit to the data of the undoped sample are $A=1.32\times10^{-43}\,\mathrm{s}^3$, $\eta=1\,\mathrm{nm}$ and $d_g(z=L)=110\,\mathrm{nm}$. The defect scattering parameter is two orders of magnitude greater than that provided to bulk single-crystal silicon samples. This indicates that the relative number of defects in the undoped single-crystal film is much greater than the defects found in the bulk material. For the doped sample the parameters that provide the best fit of the data are $A=4.38\times10^{-46}\,\mathrm{s}^3$, $\eta=0.15\,\mathrm{nm}$, and

$d_g(z = L) = 250$ nm. The defect scattering parameter is obtained from A and is based on the dopant concentration of boron, $n = 1.0 \times 10^{19}\,cm^{-3}$, as specified in the experiment conducted by McConnell *et al.* (2000). Note that the current fitting parameters are very different from those reported by McConnell *et al.* (2000) (Table VI). However, the fitting parameters reported here provide a much better fit to the data than those provided by the results of McConnell *et al.* 2000).

The fitting parameters for two boron-doped polycrystalline films in Figure 16(a) are in very good agreement with those reported by McConnell *et al.* (2001). The biggest difference, found in this study, is in the actual value of the dopant concentration used for providing the fitting parameter $A = 1.09 \times 10^{-44}\,s^3$ was of $n = 25 \times 10^{19}\,cm^{-3}$.

The fitting parameters for two phosphorus-doped polycrystalline films in Figure 16(b) are also in very good agreement with those reported by McConnell *et al.* (2001). As mentioned earlier, since N-type dopants tend to segregate to the grain boundaries, in contrast to past efforts by McConnell *et al.* (2001), the segregated scattering equation is used in addition to the grain boundary scattering equation in this study. Since it is difficult to estimate the fraction of the segregated atoms, this model assumes that 75 percent of the scattering occurs due to the grain boundaries in the grain boundary scattering equation and that 25 percent of the scattering occurs due to the segregated grain boundaries in the segregated equation.

Comparison of results between Holland model and EPRT

Figure 17 provides the theoretical fitting for the temperature-dependent thermal conductivity experimental data of doped single-crystal silicon films of thicknesses 0.42,0.83 and 1.6 μm. It is interesting to note that Holland's theory seems to predict accurately the overall behavior for films with thicknesses greater than $\sim 1\,\mu$m. Since the scattering mechanism that has more impact at lower temperatures is the grain boundary mechanism, it appears that the form of equation for grain boundary is not very appropriate for use with films thinner than 1 μm. The poor agreement of the fitting parameters with the lower temperature and smaller samples could be attributed to the fact that instead of the grain boundaries the layer boundaries will limit the thermal conductivity (McConnell *et al.*, 2001). However, a closer look at Callaway "type' models reveals that these are appropriate for diffusive results. As observed in Figure 17, it is clear that the room temperature and above room temperature data can be fitted with Holland's model. Only at low temperatures, where the ballistic issues become more predominant, the Holland's model is not in agreement with experimental results.

Figure 18(a) shows the experimental and analytical results obtained by Asheghi *et al.* (1998) for crystalline silicon layers of thicknesses 0.42, 0.83 and 1.6 μm. In their study, yet another modification to Callaway's temperature-dependent thermal conductivity model is employed which

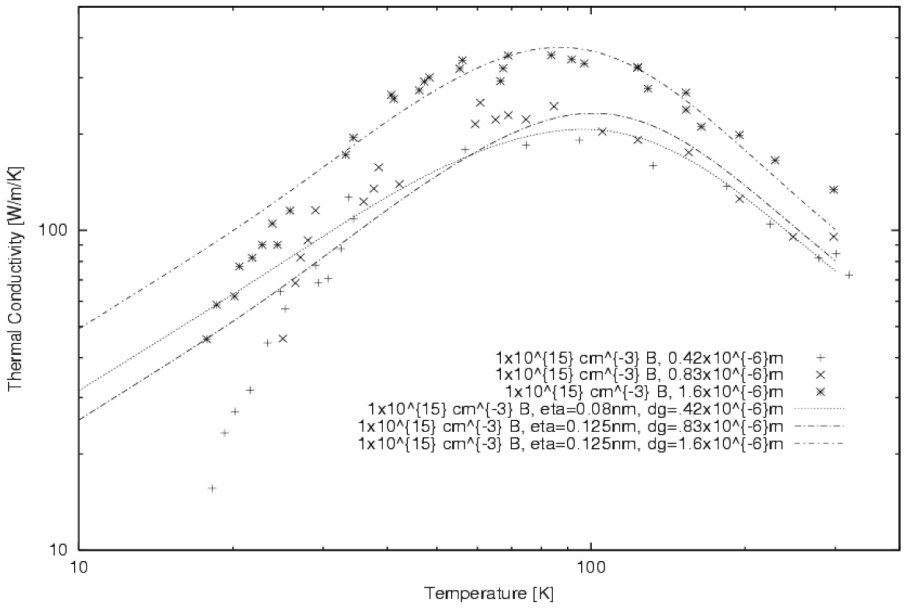

Figure 17.
Comparison of thermal conductivity of doped single-crystalline silicon films of thicknesses $L = 0.42$, 0.83 and 1.6 μm

Source: Asheghi *et al*. (1998)

considers the possibility of specular reflection through the surface. Their results show the peak in the conductivity for thin films to occur at 70 K. The recommended bulk conductivity reaches a maximum of 5,500 W/m/K at 30 K (Asheghi *et al.*, 1998).

The EPRT is one of the first models to provide accurate results when the conduction mechanism shifts from a purely diffusive to a purely ballistic mode. Therefore, Figure 18(b) shows the results from the finite-element implementation of the steady-state EPRT compared to the experimental and analytical results given by Asheghi *et al.* (1998). Although the results in Figure 18(b) present values that are higher than those seen in results of Asheghi and colleagues, it provides a better fit of the data at low temperatures. The current study of the EPRT did not include effects of grain boundary scattering. This demonstrates that the addition of the grain boundary scattering reduces the thermal conductivity by adding more sites for the thermal resistance. The results obtained by the EPRT method seem to be more appropriate to be used with films of the 1 μm range. Note that at room temperature, the mean free path of silicon and diamond films are 0.0409 and 0.39 μm, respectively. Hence, films thinner than 1 μm will present microscopic ballistic behavior at room temperature.

The results shown by using the FEM are based on experimental thermal conductivity data available from work by Anthony *et al.* (1990) (Table VIII).

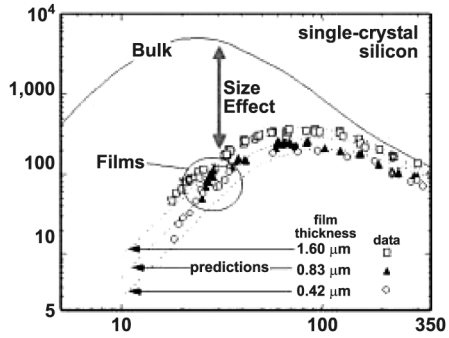

(a) Experimantal data and analytical results following Holland's method of crystalline silicon layers of several thicknesses from (Asheghi *et al.*, 1998) (with grain boundary)

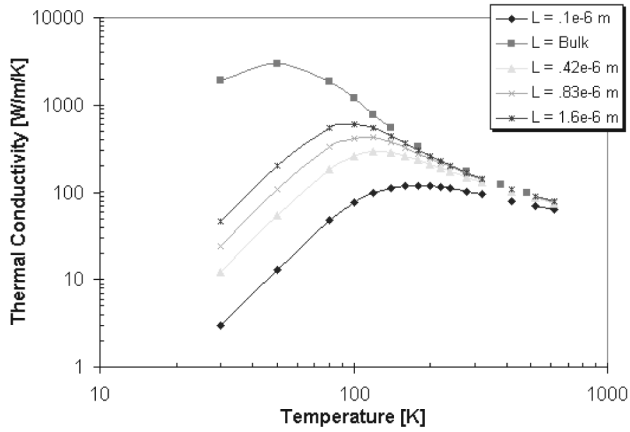

(b) FEM results following the EPRT method for silicon layers of several thicknesses (without grain boundary)

Figure 18.
Asheghi *et al.*'s work compared to the results using the FEM to solve the EPRT in determining temperature-dependent thermal conductivity for thin silicon films

Parameter	Diamond		Silicon
v (m/s)	12,288	13,500	6,500
λ (μm)	0.39	0.447	0.044
A	163.94	163.94	101.4
σ (W/m^2/K^4)	51.4995	42.415	24.8
θ_D (K)	1,860	1,860	625

Table VIII.
Parameters used in solving the EPRT for diamond and silicon films

After the heat flux results for several film thicknesses spanning both ballistic and diffusive limits were obtained, the effective thermal conductivity data for single thin films such as diamond and silicon are shown in Figure 19. Both plots are obtained by using equation (51) and results of heat flux provided by the FEM.

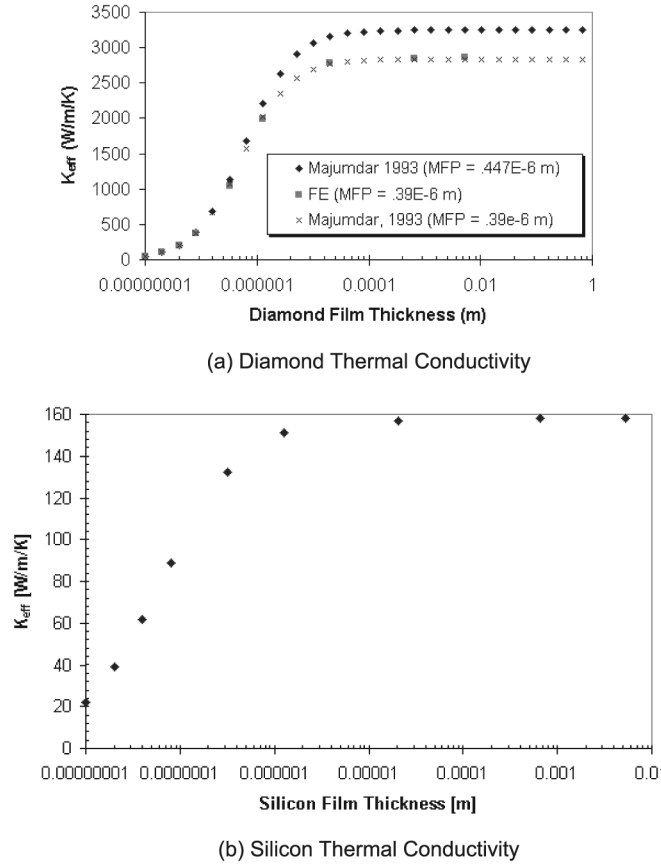

Figure 19.
Effective thermal conductivity data for single dielectric thin films by using FEM

Thermal conductivity results for diamond films asymptotically approach the bulk thermal conductivity data provided in the experiment by Anthony *et al.* (1990) where the thermal conductivity of type IIA diamond films with impurity density of $\eta_i = 0.154 \times 10^{26}\,\mathrm{m}^{-3}$ is 3,320 W/m/K. Figure 19(a) also provides thermal conductivity data at two different phonon velocities ($v = 13{,}500$ and 12,288 m/s). This change in velocity causes changes in the mean free path. It is observed that the thermal conductivity is reduced when the mean free path is reduced. This illustrates the effects of introducing more scattering mechanisms into the thin film.

Figure 19(b) provides thermal conductivity results for different silicon film thicknesses and asymptotically approaches the bulk thermal conductivity of 158 W/m/K.

Results based on the modified Callaway/Holland model

Figure 20 shows results obtained by using the modified Callaway/Holland's model for a diamond thin film. The fitting parameters in Figure 20 are

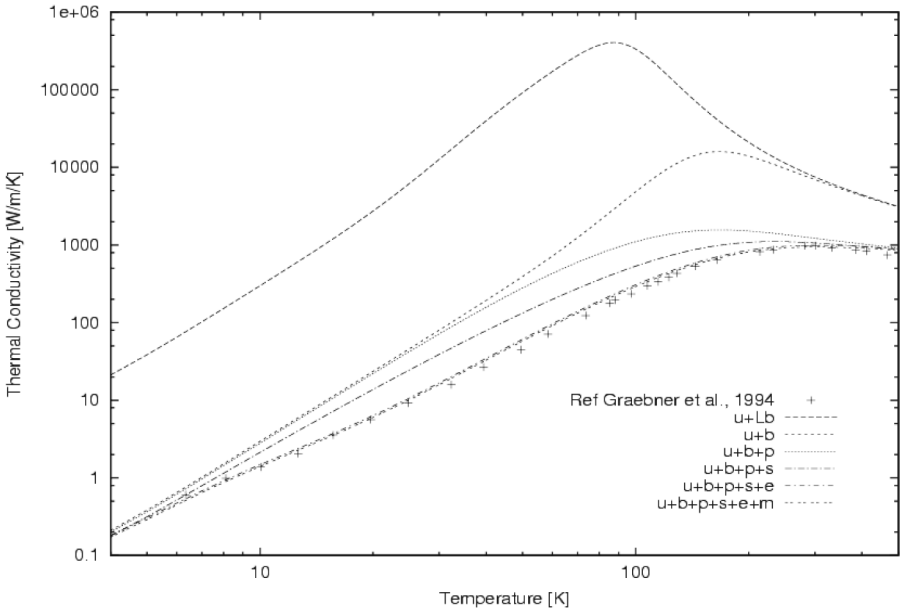

Note: (u) umklapp, (Lb) boundary for bulk films, (b) grain-boundary for thin films, (p) point defect, (s) strain, (e) extended defect, and (m) for microcracks

Source: Graebner *et al*. (1994)

Figure 20. Comparison of temperature-dependent thermal conductivity data and predictions following the theory in section for a diamond film of thickness $L = 707\,\mu$m

$A = 1.3 \times 10^{-30}\,\mathrm{s}^3$, $\eta = 10\,\mathrm{nm}$, $d_g(z = L) = 10\,\mu\mathrm{m}$ for the thin film and $d_g(z = L) = 1,000\,\mu\mathrm{m}$ for the bulk film, $c_e = 19 \times 10^{22}\,\mathrm{m}^3$, $F = 1.5\,\mathrm{nm}$, $S = 43 \times 10^{-5}$, $A_n = 7.2 \times 10^{-11} K^{-3}$, $C = 670\,\mathrm{K}$, $B_u = 1.5 \times 10^{-14}\,\mathrm{m/K}$, and $M_c = 0.94$. These results reproduce these provided by Graebner *et al.* (1994). Note that the different curves provide information on the addition of the different scattering mechanisms: (u) umklapp, (Lb) boundary for bulk films, (b) grain-boundary for thin films, (p) point defect, (s) strain, (e) extended defect, and (m) for microcracks.

Results based on MD

A lot of effort is being put forth on both experimental and theoretical retrieval of thermal conductivity of nanotubes. CNTs are proposed to be an alternative to the conventional silicon-based-microelectronics for circuits of $\sim 10\,\mathrm{nm}$ (Kreupl *et al.*, 2002). Amazingly, the thermal conductivity of nanotubes is twice that of diamond films and 15 times greater than that of copper. While normal metals can carry $\sim 10^6\,\mathrm{A/cm}^2$, SWNTs can carry up to $10^9\,\mathrm{A/cm}^2$, thus presenting itself as an excellent material for field effect transistors (FETs) (Baughman *et al.*, 2002).

Figure 21 provides experimental results of thermal conductivity of MWNTs with the room temperature value over 3,000 W/mK. Although there are three types of CNTs, thermal conductivity is determined by phonons at all temperatures (Hone *et al.*, 1999). Owing to geometrical differences between experimental set-ups of nanotube samples, there appears to exist some disagreement between reported thermal conductivity data. The reported experimental room temperature thermal conductivity for bulk bundles is 36 W/mK with deduced values for one SWNT ranging from 1,800 to 6,000 W/mK (Hone *et al.*, 1999). SWNTs usually come together to form bundles in a hexagonally arranged manner to form a crystal-like structure (Thess *et al.*, 1996). The theoretical expectation for SWNTs is of 6,000 W/mK (Berber *et al.*, 2000). A source of explanation for such discrepancy is that obtaining absolute values of thermal conductivity from bundle samples is too uncertain due to the tube-tube junction, which might be a source of barrier to the thermal conductivity transport (Kim *et al.*, 2002).

The illustrative results presented here are for an armchair SWNT based on the Tersoff-Brenner potential (Brenner, 1990) and solve the equation of motion using a predictor-corrector algorithm with fixed time steps of 0.5 fs. The (10, 10) SWNT used has 1,600 atoms (this corresponds to a nanotube with 98.4 Å), and the cross-sectional area is taken to be a ring of 3.4 Å.

In running the NEMD based on the direct method, it is important to achieve a steady-state current flow and very long simulation times are required. It was found that to achieve a smooth temperature profile for a thin film Si grain boundary system, the simulation time should be in the order of 1 ns

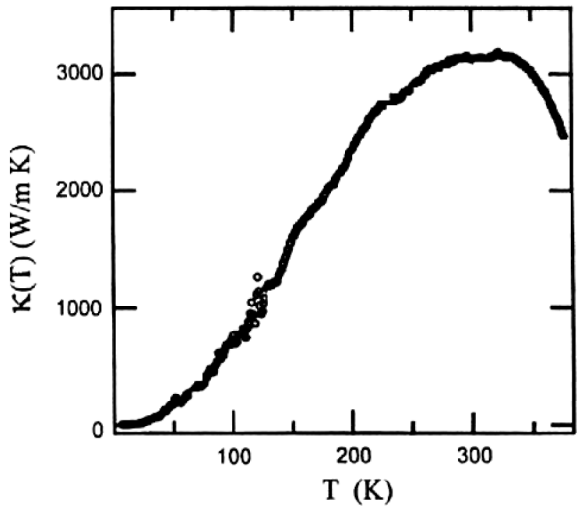

Source: Kim *et al.* (2002)

Figure 21.
Temperature-dependent thermal conductivity of MWNTs with diameter $d = 14$ nm and length $l = 2.5\ \mu$m

(Schelling *et al.*, 2002). Although this would correspond to 2×10^6 MD steps for the 0.5 fs time steps used in the simulation analysis, only 5×10^4 steps were used in the illustrative results presented here.

The results shown in Figure 22 are the running average temperatures in the thin slices over 5×10^4 MD steps.Owing to sharp deviations from the linear gradient at the edges, the gradient of the temperature is obtained from the slabs in the middle of the simulation. The running averages between 5×10^4 and 1×10^5 are compared to determine whether the simulation has reached equilibrium.

As found in results conducted to thin films, the expected trend in the temperature-dependent thermal conductivity for CNTs is that at lower temperatures, the thermal conductivity is low, as the temperature increases it reaches a maximum, and then it starts to decrease at higher temperatures. The peak of the thermal conductivity was found to be dependent on the diameter of the SWNT. This overall trend is found for SWNTs in the work conducted by Osman and Srivastava (2001). It is worth noting that the nanotubes studied in Osman and Srivastava (2001) range from 151 to 221 Å with imposed periodic boundary conditions, while the nanotube studied here is 98.4 Å with rigid boundary conditions. Osman and Srivastava found that the thermal conductivity is highly dependent on the tube diameter but is independent of the tube chirality. The room temperature thermal conductivity for the (10,10) tube with length 98.4 Å is found to be 1,040 W/mK after 5×10^4 MD steps which

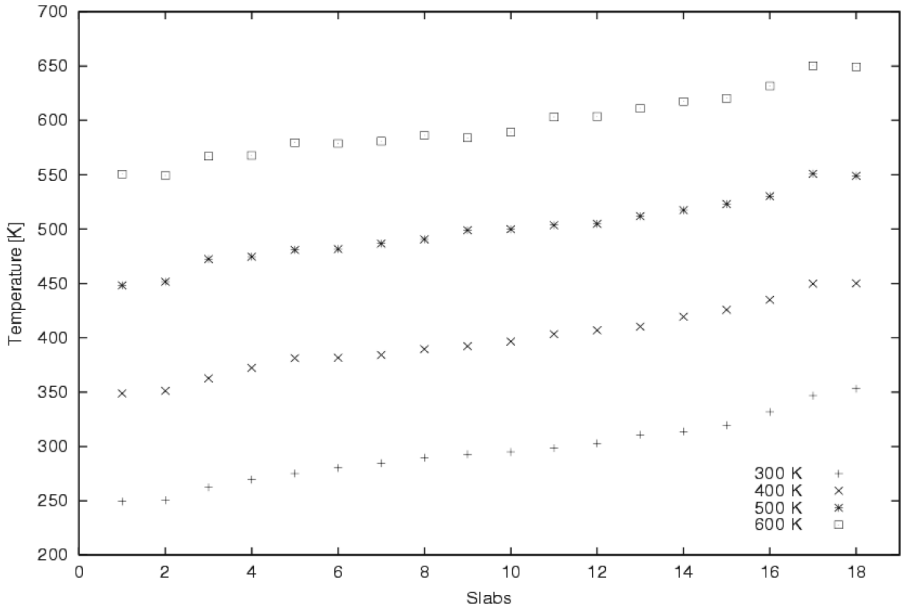

Figure 22.
Typical temperature profile obtained from MD simulations with running average over 5×10^4 time steps

is smaller than that reported (~1,600 W/mK) by Osman and Srivastava (2001). This difference is consistant with size effects.

Concluding remarks

The temperature-dependent thermal conductivity theory originally developed by Callaway (1959) and later modified by Holland (1963) and the steady-state EPRT are used in this overview in order to test experimental results provided by several researchers for doped and undoped single- and polycrystalline thin dielectric films such as silicon and diamond. When using Holland's model it is assumed that the scattering mechanisms present for both doped and undoped samples are U- and N-processes, grain boundaries, and defects. The fitting parameters common to all cases are the defect scattering parameter A, the rms grain boundary surface roughness η, and the maximum grain size $d_g(z = L)$.

It is noteworthy to mention that the scattering theory presented here was able to provide good fitting approximations to most of the data of the silicon films. In the case of single-crystal silicon films, a slight modification to the definition of d_g is needed in order to use the grain boundary equation. In the case of *single-crystal* films, d_g is the film thickness (dimension parallel to the heat flow) and in the case of *polycrystalline* films d_g is the average distance between the intersections of grain boundaries with a straight line drawn on a top-view electron micrograph of the film (dimension perpendicular to the heat flow).

The experimental data show that the thermal conductivity of thin dielectric films can be one to two orders of magnitude lower than that of the bulk materials (Graebner *et al.*, 1993; Lambropoulos *et al.*, 1989). This has pushed the area of thermophysical prediction of thin dielectric films into the 21st century. The well-documented and studied Fourier law was not able to explain these experimental observations. Hence, other methods to predict the thermal conductivity of thin films are being developed. The Cattaneo model was able to explain the small-time behavior of experiments performed at cryogenic temperatures. The EPRT (Majumdar, 1993) was able to explain the small-time (Joshi and Majumdar, 1993) and spatial variations of thin dielectric films. Solutions to this method have been proposed (Jen and Chieng, 1998; Majumdar, 1993; Siegel and Howell, 1992), and the present study develops the FEM.

Note that the FEM study of the EPRT identified deficiencies regarding the heat flux computations that had not been reported previously (Anderson and Tamma, 2002). While oscillations are observed for the FEM, they are quickly removed by increasing the number of grid points. Although other stabilizing techniques were attempted (i.e. upwinding), they did not remove the oscillatory behavior, and further study is underway.

In understanding the different mechanisms of heat conduction in solids, the C- and F-processes model is also depicted in order to provide a bridge between

the slow Cattaneo (C-processes) and the fast Fourier (F-processes) limits. The postulation used to describe the C- and F-processes model stems from the understanding that within the distribution functions that arise from each carrier processes, there exists a threshold frequency which separates high and low energy processes.

By using the premise that there exists a threshold frequency separating the low and high energy processes, emanating from the C- and F-processes model, the Jeffreys model is, for the first time, also derived from the BTE. It is important to be clear about the differences between the C- and F-processes and the Jeffreys model. The Jeffreys model was originally thought to be a linear combination of the Fourier and Cattaneo models (Tamma and Zhou, 1998); however, further investigations lead to the fact that the Jeffreys model can only recover the Cattaneo model and a Fourier-like model with relaxation (Anderson, 2001). On the other hand, the C- and F-processes model is the first to recover exactly both the Fourier and Cattaneo models and to provide meaningful physical explanation to the Jeffreys model as well to introduce the dimensionless heat conduction model number. When the combined form of the C- and F-processes model is used in the energy equation, it leads to the generalized one-step temperature equation given by the Jeffreys model.

Although the prediction of thermal conductivity in thin dielectric films is well-developed using Holland's and EPRT methods, detailed information on the microstructure is needed for making the correct prediction of the scattering rate times difficult. Often an experiment is needed for validating these models. It appears that the MD method is more appropriate for use in determining the thermal conductivity considering that the relaxation time is not needed and also because of the ability to address the microstructural elements of different material, especially polycrystalline films (Schelling *et al.*, 2002).

CNTs are an emerging source of several possibilities for applications in several areas: carbon nanotube composites, electrochemical devices, hydrogen storage, fuel cells, field emission devices, nanometer-sized electronic devices, and sensors and probes (Baughman *et al.*, 2002). The area has grown remarkably in its 12 year existence and many more interesting applications are likely to emerge.

In summary, the Fourier law is only valid in the macroscopic regimes for both time and size domains. The Cattaneo and Jeffreys model although being valid for microscopic time domains are only valid for macroscopic size domains. The EPRT is valid for both microscopic time (Joshi and Majumdar, 1993) and size domains. Another model that possesses the ability to span the microscopic time and size domains is the BD equation (Chen, 2001). It is interesting to note that similar assumptions made by the C- and F-Processes model are made in the BD model.

References

Anderson, C.V.D.R. (2001), "Microscale heat conduction theory – an in depth look at the Boltzmann transport equation and a finite-element formulation for the prediction of thermal conductivity of thin dielectric films", Master's thesis, University of Minnesota.

Anderson, C.V.D.R. and Tamma, K.K. (2002), "Evaluation of numerical approximation techniques for determination of micro and macroscale conductivity in thin dielectric films", *Presented at the AIAA – Thermophysics Section*, pp. 1-11.

Anthony, T.R., Banholzer, W.F., Fleischer, J.F., Wei, L., Kuo, P.K., Thomas, R.L. and Pryor, R.W. (1990), "Thermal diffusivity of isotropically enriched 12c diamond", *Physical Review B*, Vol. 42, pp. 1104-11.

Asen-Palmer, M., Bartkowski, K., Gmelin, E., Cardona, M., Zhernov, A.P., Inyushkin, A.V., Taldenkov, A., Ozhogin, V.I., Itoh, K.M. and Haller, E.E. (1997), "Thermal conductivity of germanium crystals with different isotopic compositions", *Physical Review B*, Vol. 56 No. 15, pp. 9431-47.

Ashcroft, N.W. and Mermin, N.D. (1976), *Solid State Physics*, W.B. Saunders, Philadelphia.

Asheghi, M., Touzelbaev, M.N., Goodson, K.E., Leung, Y.K. and Wong, S.S. (1998), "Temperature-dependent thermal conductivity of single-crystal silicon layers in soil substrates", *Transactions of the ASME*, Vol. 120, pp. 30-6.

Baughman, R.H., Zakhidov, A.A. and de Heer, W.A. (2002), "Carbon nanotubes – the route toward applications", *Science*, Vol. 297, pp. 787-92.

Berber, S., Kwon, Y-K. and Tománek, D. (2000), "Unusually high thermal conductivity of carbon nanotubes", *Physical Review Letters*, Vol. 84 No. 20, pp. 4613-6.

Berman (1992), "Thermal conductivity of isotopically enriched diamonds", *Physical Review B*, Vol. 45 No. 10, pp. 5726-8.

Brenner, D.W. (1990), "Empirical potential for hydrocarbons for use in simulating the chemical vapor deposition of siamond films", *Physical Review B*, Vol. 42 No. 15, pp. 9458-71.

Brenner, D.W. (1997), "Analytic potential and molecular dynamics simulation", *Presented at the Fifth Foresight Conference on Molecular Nanotechnology*.

Callaway, J. (1959), "Model of lattice thermal conductivity at low temperatures", *Physical Review*, Vol. 113 No. 4, pp. 1046-51.

Che, J., Çağin, T., Deng, W. and Goddard III, W.A. (2000), "Thermal conductivity of diamond and related materials from molecular dynamics simulations", *Journal of Chemical Physics*, Vol. 113 No. 16, pp. 6888-900.

Chen, G. (1997), "Size and interface effects on thermal conductivity of superlattices and periodic thin-film structures", *ASME Journal of Heat Transfer*, Vol. 119, pp. 220-9.

Chen, G. (1998), "Thermal conductivity and ballistic phonon transport in cross-plane direction of superlattices", *Physical Review B*, Vol. 57, pp. 14958-73.

Chen, G. (2000), "Phonon heat conduction in nanostructures", *International Journal of Thermal Sciences*, Vol. 39, pp. 471-80.

Chen, G. (2001), "Ballistic-diffusive heat-conduction equations", *Physical Review Letters*, Vol. 86 No. 11, pp. 2297-300.

Chen, G. and Tien, C.L. (1993), "Thermal conductivity of quantum well structures,", *Journal of Thermophysics and Heat Transfer*, Vol. 7 No. 2, pp. 311-8.

Ercolessi, F. (1997), *A Molecular Dynamics Primer*, Spring College in Computational Physics, ICTP, Trieste.

Evans, D.J. and Morriss, G.P. (1990), *Statistical Mechanics of Nonequilibrium Liquids*, Theoretical Chemistry Monograph Series, Academic Press, New York, NY.

Goodson, K.E. (1996), "Thermal conductivity in nonhomogeneous CVD diamond layers in electronic microstructures", *Journal of Heat Transfer*, Vol. 118, pp. 279-86.

Goodson, K. and Flik (1992), "Microscale phonon transport in dielectrics and intrinsic semiconductors", *HTD – Fundamental Issues in Small Scale Heat Transfer – ASME*, Vol. 227, pp. 29-36.

Goodson, K.E., Kading, O.W., Rosler, M. and Zachai, R. (1995), "Experimental investigation of thermal conductivity normal to diamond-silicon boundaries", *J. Appl. Phys.*, Vol. 77 No. 4, pp. 1385-92.

Graebner, J.E., Jin, S., Kammlott, G.W., Wong, Y.H., Herb, J.A. and Gardinier, C.F. (1993), "Thermal conductivity and the microstructure of state-of-the-art cvd diamond", *Diamond and Related Materials*, Vol. 2, pp. 1059-63.

Graebner, J.E., Reiss, M.E., Seibles, L., Hartnett, T.M., Miller, R.P. and Robinson, C.J. (1994), "Phonon scattering in chemical-vapor-deposited diamond", *Physical Review B*, Vol. 50 No. 6, pp. 3702-13.

Haile, J.M. (1992), *Molecular Dynamics Simulation: Elementary Methods*, Wiley, New York, NY.

Holland, M.G. (1963), "Analysis of lattice thermal conductivity", *Physical Review*, Vol. 132 No. 6, pp. 2461-71.

Hone, J., Whitney, M. and Zettl, A. (1999), "Thermal conductivity of single-walled carbon nanotubes", *Synthetic Metals*, Vol. 103, pp. 2498-9.

Hook, J.R. and Hall, H.E. (1991), *Solid State Physics*, 2nd ed., Wiley, New York, NY.

Iijima, S. (1991), "Helical microtubules of graphitic carbon", *Nature*, Vol. 354, pp. 56-8.

Iijima, S. (2002), "Carbon Nanotubes: past, present, and future", *Physica B*, Vol. 323, pp. 1-5.

Iijima, S. and Ichihashi, T. (1993), "Single shell carbon nanotubes of one nanometer diameter", *Nature*, Vol. 363, pp. 503-605.

Jen, C-P. and Chieng, C-C. (1998), "Microscale thermal characterization for two adjacent dielectric thin films", *Journal of Thermophysics and Heat Transfer*, Vol. 12 No. 2, pp. 146-52.

Joseph, D.D. and Preziosi, L. (1989), "Heat waves", *Rev. Mod. Phys.*, Vol. 61 No. 1, pp. 41-73.

Joshi and Majumdar (1993), "Transient ballistic and diffusive phonon heat transport in thin films", *J. Appl. Phys.*, Vol. 74 No. 1, pp. 31-9.

Kim, P., Shi, L., Majumdar, A. and McEuen, P. (2002), "Mesoscopic thermal transport and energy dissipation in carbon nanotubes", *Physica B*, Vol. 323, pp. 67-70.

Kittel, C. (1996), *Introduction to Solid State Physics*, 6th ed., Wiley, New York, NY.

Klemens, P.G. (1955), "The scattering of low-frequency lattice waves by static imperfections,", *Proc. Phys. Soc. A*, Vol. 68, pp. 1113-28.

Kreupl, F., Graham, A. and Hönlein, W. (2002), "A status report on technology for carbon nanotube devices", *Solid State Technology*, pp. S9-S16.

Kumar, S., Majumdar, A. and Tien, C.L. (1990), "The differential-discrete-ordinate method for solutions of the equation of radiative transfer", *Transactions of the ASME*, Vol. 112, pp. 424-5.

Lambropoulos, J.C., Jacobs, S.D., Burns, S.J., Shaw-Klein, L. and Hwang, S.S. (1991), "Thermal conductivity of thin films: measurement and microstructure effects", *HTD – Thin Film Heat Transfer: Properties and Proceedings ASME*, Vol. 184, pp. 21-32.

Lambropoulos, J.C., Jolly, M.R., Amsden, C.A., Gilman, S.E., Sinicropi, M.J., Diakomihalis, D. and Jacobs, S.D. (1989), "Thermal conductivity of dielectric thin films", *J. Appl. Phys.*, Vol. 66 No. 9, pp. 4230-42.

Lee, J.F., Sears, F.W. and Turcotte, D.L. (1973), *Statistical Thermodynamics*, 2nd ed., Addison-Wesley, Reading, MA.

Lukes, J.R., Li, D.Y., Liang, X-G. and Tien, C-L. (2000), "Molecular dynamics study of solid thin-film thermal conductivity", *Journal of Heat Transfer*, Vol. 122, pp. 536-43.

Majumdar, A. (1991), "Microscale heat conduction in dielectric thin films", *HTD – Thin Film Heat Transfer: Properties and Processing ASME*, Vol. 184, pp. 33-42.

Majumdar, A. (1993), "Microscale heat conduction in dielectric thin films", *Journal of Heat Transfer*, Vol. 115, pp. 7-16.

Maruyama, S. (2000), *Advances in Numerical Heat Transfer*, Chapter 6., Vol. 2, Taylor and Francis, New York, NY.

Maruyama, S. (2002), "A molecular dynamics simulation of heat conduction in finite length swnts", *Physica B*, Vol. 323, pp. 193-5.

McConnell, A.D., Uma, S. and Goodson, K.E. (2000), "Thermal conductivity of doped polysilicon layers", *Proceedings of the International Conference on Heat Transfer and Transport Phenomena in Microscale Structures*, pp. 413-9.

McConnell, A.D., Uma, S. and Goodson, K.E. (2001), "Thermal conductivity of doped polysilicon layers", *Journal of Microelectromechanical Systems*, Vol. 10, pp. 360-9.

Muller-Plathe, F. (1997), "A simple nonequilibrium molecular dynamics method for calculating the thermal conductivity", *J. Chem. Phys.*, Vol. 106 No. 14, pp. 6082-5.

Olson, J.R., Pohl, R.O., Vandersande, J.W., Zoltan, A., Anthony, T.R. and Banholzer, W.F. (1993), "Thermal conductivity of diamond between 170 and 1200 K and the isotope effect", *Physical Review B*, Vol. 47 No. 22, pp. 14850-6.

Osman, M.A. and Srivastava, D. (2001), "Temperature dependence of the thermal conductivity of single-wall carbon nanotubes", *Nanotechnology*, Vol. 12, pp. 21-4.

Özisik, M.N. (1973), *Radiative Transfer and Interactions with Conduction and Convection*, Wiley, New York, NY.

Rapaport, D.C. (1995), *The Art of Molecular Dynamics Simulation*, Cambridge University Press, Cambridge.

Razzaque, M.M., Howell, J.R. and Klein, D.E. (1984), "Coupled radiative and conductive heat transfer in a two-dimensional rectangular enclosure with gray participating media using finite elements", *J. Heat Transfer*, Vol. 106 No. 3, pp. 613-9.

Saito, R., Fujita, M., Dresselhaus, G. and Dresselhaus, M.S. (1992), "Electronic structure of chiral graphene tubules", *Applied Physics Letters*, Vol. 60 No. 18, pp. 2204-6.

Schelling, P.K., Phillpot, S.R. and Keblinski, P. (2002), "Comparison of atomic-level simulation methods for computing thermal conductivity", *Physical Review B*, Vol. 65, pp. 144306-1-144306-12.

Siegel, R. and Howell, J.R. (1992), *Thermal Radiation Heat Transfer*, 3rd ed., Hemisphere Publishing Corp., New York, NY.

Sparrow, E. (1991), *Thermal Radiation Heat Transfer*, 2nd ed., Hemisphere Publishing Corp., New York, NY.

Stillinger, F.H. and Weber, T.A. (1985), "Computer simulation of local order in condensed phases of silicon", *Physical Review B*, Vol. 31 No. 8, pp. 5262-71.

Stote, R., Dejaegere, A., Kuznetsov, D. and Falguet, L. (1999), "Theory of molecular dynamics simulations", Available at: http://www.ch.embnet.org/MD_tutorial/

Swartz, E.T. and Pohl, R.O. (1989), "Thermal boundary resistance", *Review of Modern Physics*, Vol. 61, pp. 605-68.

Tamma, K.K. and Zhou, X. (1998), "Macroscale and microscale thermal transport and thermo-mechanical interactions: some noteworthy perspectives", *Journal of Thermal Stresses*, Vol. 21, p. 405.

Tersoff, J. (1988a), "Empirical interatomic potential for silicon with improved elastic properties", *Physical Review B*, Vol. 38 No. 14, pp. 9902-5.

Tersoff, J. (1988b), "New emperical approach for the structure and energy of covalent systems", *Physical Review B*, Vol. 38 No. 12, pp. 6991-7000.

Thess, A., Lee, R., Nikolaev, P., Dai, H., Petit, P., Robert, J., Xu, C., Lee, Y.H., Kim, S.G., Rinzler, A.G., Colbert, D.T., Scuseria, G.E., Tománek, D., Fischer, J.E. and Smalley, R.E. (1996), "Crystalline ropes of metallic carbon nanotubes", *Science*, Vol. 273, pp. 483-7.

Vincenti, W.G. and Kruger, C.H. (1977), *Introduction to Physical Gas Dynamics*, Robert Krieger, New York, NY.

Volz, S.G. and Chen, G. (1999), "Molecular dynamics simulation of thermal conductivity of silicon nanowires", *Applied Physics Letters*, Vol. 75 No. 14, pp. 2056-8.

Wildöer, J.W.G., Venema, L.C., Rinzler, A.G., Smalley, R.E. and Dekker, C. (1998), "Electronic structure of atomically resolved carbon nanotubes", *Nature*, Vol. 391, pp. 59-62.

Yang, R. and Chen, G. (2001), "Two-dimensional nanoscale heat conduction using ballistic-diffusive equations", *Presented at International Mechanical Engineering Congress – ASME*.

Zeghbroeck, B.J.V. (1996), "Distribution functions", Available at: http://ece-www.colorado.edu/~bart/book/distrib.htm#thermo

Zeng, T. and Chen, G. (2001), "Phonon heat conduction in thin films: impacts of thermal boundary resistance and internal heat generation,", *Journal of Heat Transfer*, Vol. 123, pp. 340-7.

Zhigilei, L.V. (2002), "Mse 524: modeling in materials science", Available at: http://www.people.virginia.edu/l z2n/mse524/

Zhou, X., Tamma, K.K. and Anderson, C.V.D.R. (2001), "On a new c- and f-processes heat conduction constitutive model and the associated generalized theory of thermoelasticity", *Journal of Thermal Stresses*, Vol. 24, pp. 531-64.

Ziman (1960), *Electrons and Phonons: The Theory of Transport Phenomena in Solids*, Clarendon Press, Oxford.